1   # Retrieval Algorithm for Aerosol Effective Height from the

2   # Geostationary Environment Monitoring Spectrometer (GEMS)

4   Sang Seo Park[1,*], Jhoon Kim[2], Yeseul Cho[2], Hanlim Lee[3], Junsung Park[3], Dong-Won

5   Lee[4], Won-Jin Lee[4], Deok-Rae Kim[4]

6   [1] *Department of Urban and Environmental Engineering, Ulsan National Institute of Science*

7   *and Technology, Ulsan, Korea*

8   [2]*Department of Atmospheric Sciences, Yonsei University, Seoul, Korea*

9   [3]*Division of Earth and Environmental System Sciences, Pukyong National University, Busan,*

10   *South Korea*

11   [4]*Envionment Satellite Center, National Institute of Environmental Research, Incheon, Korea*

15   *Corresponding author. Sang Seo Park (sangseopark@unist.ac.kr)

18   Submitted to Atmospheric Measurement Techniques

19   2023. 06.

Abstract

An algorithm for aerosol effective height (AEH) was developed for operational use with observations from the Geostationary Environment Monitoring Spectrometer (GEMS). The retrieval technique uses the slant column density of the oxygen dimer (O_2-O_2) at 477 nm, which is converted into AEH after retrieval of aerosol and surface optical properties from GEMS operational algorithms. The retrieved AEHs provide continuous vertical information of severe dust plumes over East Asia with reasonably good validation results and the collection of plume height information for anthropogenic aerosol pollutants over India. Compared to the AEH retrieved from Cloud-Aerosol Lidar with Orthogonal Polarization (CALIOP), the retrieval results show bias of -0.03 km with a standard deviation of 1.4 km for the AEH difference over the GEMS observation domain from January to June, 2021. The AEH difference depends on aerosol optical properties and surface reflectance. Compared to the aerosol layer height obtained from the tropospheric monitoring instrument (TROPOMI), differences of 1.50 ± 1.08 km, 1.59 ± 1.22 km, and 1.71 ± 1.24 km were obtained for pixels with single scattering albedo (SSA) < 0.90, 0.90 < SSA < 0.95, and SSA > 0.95, respectively.

Keywords: aerosol effective height, aerosol optical depth, environmental satellite, GEMS

1. Introduction

Since the launch of the Total Ozone Mapping Spectrometer (TOMS) on Nimbus-7, ultraviolet (UV)-visible satellite measurements have been used for environmental monitoring of the distribution and reaction processes of pollutants (e.g., anthropogenic aerosols, tropospheric ozone, NO_2, and SO_2). Measurements from environmental satellites have been used to estimate gaseous species in the atmosphere, resulting in vertical column integrated amounts. However, these column-integrated amounts and associated surface concentrations have uncertainty due to simultaneous changes in optical path length associated with the vertical distribution of target species and amounts of scattering materials (clouds and aerosols) present. In addition, aerosol vertical information is also important for the application of tropospheric concentration of aerosols. For example, aerosol height information in the free troposphere is particularly important for aviation safety by affecting the visibility. Also, scientific applications including radiative forcing studies, long-range transport modelling and studies of cloud formation processes have been used aerosol vertical information as an input parameter.

Environmental satellite sensors, that measure UV-visible wavelength, have been used the UV aerosol index (UVAI) for aerosol detection (e.g., Buchard *et al.*, 2015; Herman *et al.*, 1997; Torres *et al.*, 1998, 2002; Prospero *et al.*, 2000; de Graaf *et al.*, 2005). Furthermore, scattering radiative index values were investigated for the possibility of the cloud signal detection (Penning de Vries *et al.*, 2009, 2015; Kooreman *et al.*, 2020; Kim *et al.*, 2018). However, these indices only have qualitative characteristics and limitations to identify aerosol amounts.

For the quantitative estimation, measurements of aerosol optical depth (AOD) and

67 radiative cloud fraction have also been retrieved from pixel-based radiance data in UV-

68 visible wavelength range. Recently, various aerosol retrieval algorithms have been

69 developed to be applied in passive satellite sensors. These algorithms focus on

70 improved trace gas retrieval as well as direct monitoring of aerosol properties, such as

71 AOD and single scattering albedo (SSA) (e.g., Ahn *et al.*, 2014; Kim *et al.*, 2020; Torres

72 et al., 2020).

73   Although the algorithms developed for environmental satellite sensors indicate the

74 presence and amounts of scattering materials, the accuracy of these retrieval algorithms

75 for trace gases is affected by the relative vertical distributions between trace gases and

76 scattering materials (e.g., Lorente *et al.*, 2017; Hong *et al.*, 2017). For this reason,

77 estimating cloud vertical parameters is important. For cloud vertical information, cloud

78 height information has been estimated simultaneously with cloud optical depth and

79 radiative cloud fraction data using the rotational Raman scattering (Joiner and Vasilkov,

80 2006; Vasilkov *et al.*, 2008; Joiner and Bhartia, 1995) and absorption intensity of the

81 oxygen dimer (O_2-O_2) (Accarreta *et al.*, 2004; Vasilkov *et al.*, 2018; Choi *et al.*, 2021)

82 combined with normalized radiance.

83   Similarly, the aerosol vertical distribution can be estimated using the oxygen

84 absorption bands, such as the O_2-O_2 (Park *et al.*, 2016; Chimot *et al.*, 2017; Choi *et al.*,

85 2019, 2020), O_2-A (Dubisson *et al.*, 2009; Geddes and Boesch, 2015; Sanders *et al.*,

86 2015; Xu *et al.*, 2017; Zeng *et al.*, 2020), and O_2-B (Chen *et al.*, 2021; Ding *et al.*,

87 2016) bands, as well as combinations of these bands (Sanghavi *et al.*, 2012; Chen *et al.*,

88 2021). In addition, an algorithm for aerosol vertical information has been developed

89 based on hyperspectral UV-visible radiance from satellite observation. Nanda *et al.*

90 (2018) demonstrated the possibility of aerosol height retrieval from the O_2-A band

developed an algorithm using Tropospheric Monitoring Instrument (TROPOMI) (Sanders and de Haan, 2016; Nanda *et al.*, 2020) and implemented the algorithm operationally.

However, the vertical distribution of aerosol is difficult to assess because of its large spatio-temporal variability. Although the Cloud-Aerosol Lidar with Orthogonal Polarization (CALIOP) provided the aerosol vertical distribution with high vertical resolution (Omar et al., 2009), other passive satellite sensors are only able to estimate the representative parameter of aerosol height. Veihelmann et al. (2007) showed that the number of degrees of freedom of signal for aerosol is 2-4 for most satellite observation conditions by the ozone monitoring instrument (OMI). In addition, the number of degrees of freedom is not exceeded to 3 from the shortwave satellite measurements (e.g., Rao et al., 2019; Choi et al., 2021). It means that the amount of information for aerosol vertical distribution has a limitation for satellite sensors. Because of limitation for describing the aerosol vertical information, aerosol layer height (ALH) (e.g., Nanda et al., 2018) or aerosol effective height (AEH) (Park et al., 2016) were defined to retrieve the aerosol vertical information from the passive satellite sensors.

The Geostationary Environment Monitoring Spectrometer (GEMS), which was launched by South Korea in February 2020, provides column density of ozone, aerosol, and their precursors (Kim *et al.*, 2020). The main purpose of GEMS is to monitor air quality, and aerosol properties are targets of such monitoring over East Asia. For this reason, the GEMS aerosol algorithm was developed as multiple operational products. The Aerosol algorithm adopted optimal estimation method (Rogers, 2000) to retrieve AOD, SSA, and ALH. Aerosol properties are obtained for the purposes of monitoring air quality and aerosol effects for the air mass factor (AMF) calculation. In addition to

115   these aerosol products, AEH is provided to represent the upper layer of the peak. Both

116   ALH and AEH help understand the vertical structure of aerosol layer. For the possibility

117   for development of an AEH retrieval algorithm, Park *et al.* (2016) conducted theoretical

118   sensitivity testing of AEH retrieval using solely the O_2-O_2 absorption band along with

119   aerosol and surface properties. Overall, the sensitivity of AEH retrieval was strongly

120   affected by SSA, AOD, and aerosol types including optical and size properties. In

121   addition, case studies of AEH during dust transport over East Asia were conducted

122   using radiance data from the Ozone Monitoring Instrument (OMI) and aerosol optical

123   properties from the Moderate Resolution Imaging Spectroradiometer (MODIS).

124   Based on theoretical considerations and case study results, we introduce an

125   operational retrieval algorithm for AEH. Section 2 introduces the details of satellite

126   sensors for the comparison and colocation method in this study. Section 3 describes the

127   details of the AEH retrieval algorithm for GEMS and provides a list of the detailed input

128   parameters. Section 4 reports retrieval results based on case studies of aerosol transport,

129   and section 5 contains long-term validation results based on CALIOP and TROPOMI

130   data. Finally, in section 6, the summary and main conclusions are presented.

131

132   **2. Data**

133   **2.1 GEMS**

134   The GEMS instrument on board the Geostationary Korea multipurpose satellite 2B

135   (GK2B) is located at 128.2°E, and scans from 145°E to 75°E with north-south coverage

136   of 5°S-45°N. The GK2B observation schedule shares the GEMS and the Geostationary

137   Ocean Color Imager 2 (GOCI2), and the GEMS scan the 30 minutes duration from

138   every hour from 45 minutes to 15 minutes during daytime. The spatial resolution of

139 GEMS is 3.5 km (North-South) × 8 km (East-West) for aerosol and gaseous products at

140 38°N. The spectral range of 300-500 nm is covered with a spectral resolution (as

141 defined by the full-width and half-maximum of the spectral response function) of 0.6

142 nm and a spectral sampling of 0.2 nm.

143 The GEMS Level 2 aerosol operational algorithm (L2AERAOD) retrieves the aerosol

144 index (AI) values for UV and visible wavelengths, as well as AOD and SSA after

145 determining the aerosol types (National Institute of Environmental Research, 2020). The

146 aerosol types are defined as absorbing, non-absorbing, and dust types by using the AI

147 based classification methods exploiting measurements in the UV and visible (e.g., Go et

148 al., 2020). Park *et al.* (2016) noted that the error budget of AEH is significantly affected

149 by uncertainty in AOD and SSA and by the misclassification of aerosol types, which is

150 directly related to the optical property and size information. Overall, uncertainties of 0.2

151 in AOD, of 20% in particle size, of 10% in SSA, and 0.02 in surface albedo cause AEH

152 errors in the range 739-1276 m (Park et al., 2016). In this study, the L2AERAOD results

153 for AOD at 550 nm and SSA at 443 nm were adopted as input data for aerosol

154 properties, and the AOD and SSA values were spectrally converted to those values at

155 assumed wavelength for the inversion calculation process after considering the spectral

156 dependence of the aerosol optical properties by the aerosol models. In addition, we also

157 used the minimum reflectance under the Lambertian assumption to retrieve AOD and

158 AEH to coincide with the use of surface information on L2AERAOD and AEH retrieval.

159

160 **2.2. TROPOMI**

161 TROPOMI is a nadir-viewing spectrometer, the only payload of the Sentinel-5

162 Precursor (S5P), measuring radiance in the UV, visible, near-infrared, and the shortwave

163 IR (Veefkind et al., 2012). The S5P is a polar orbit satellite that crosses the equator at

164 13:30 local time at an ascending node. The aerosol layer height product from

165 TROPOMI (AER_LH) provides vertically localized aerosol layers in the free

166 troposphere with cloud free condition by using the level 1b earth radiance

167 measurements from 758 to 770 nm (de Graaf *et al.*, 2022). The definition of ALH from

168 TROPOMI is the optical centroid layer height of the plume above sea level. The

169 spectral fit employs a fast forward model based on a neural network for simulated

170 condition of reflectance around the O_2-A band. After cloud masking, an optimal

171 estimation method is used to retrieve the ALH and AOD by the inversion method from

172 observation. Other aerosol parameters, such as SSA, layer thickness, and scattering

173 phase function, are assumed to be fixed values (Nanda et al., 2020). Furthermore, the

174 ALH retrieval has limitation to the aerosol plume with higher than 12 km, because the

175 ALH neural network product currently provides the plume pressure range of 75-1000

176 hPa (Michailidis et al., 2023).

177   The main purpose of the AER_LH product is the retrieval of aerosol layers in the free

178 troposphere (desert dust, biomass burning, and volcanic ash) (Michailidis et al., 2023).

179 The target requirement on the accuracy and precision is 0.5 km or 50 hPa, and the

180 threshold requirement is 1 km or 100 hPa under the elevated aerosol plumes with cloud-

181 free conditions for the layer height and for the associated pressure, respectively (de

182 Graaf et al., 2022, Veefkind et al., 2012). However, the TROPOMI ALH product has

183 strong dependence of the surface albedo, especial to the bright surfaces (Sanders et al.,

184 2015). From Michailidis et al. (2023), a mean bias of -0.51±0.77 and -2.27±1.17 km is

185 estimated over ocean and land, respectively. In this study, we use version 02.04.00 of

186 the TROPOMI offline level 2 AER_LH product (European Space Agency, 2021) with

187 the spatial resolution is 3.5 km × 5.5 km at nadir viewing geometry.

188

2.3. CALIOP

190 The CALIOP is a spaceborne lidar onboard the Cloud-Aerosol Lidar and Infrared

191 Pathfinder Satellite Observations (CALIPSO) to measure the vertical information of

192 aerosol and cloud with estimating the optical properties. The CALIOP has two different

193 wavelength channels (532 and 1064 nm) by using the Nd:YAG laser to generate the

194 signals (Winker et al., 2009). The CALIPSO is Sun synchronous orbit constellated to

195 the A-train with period of 98.3 minutes. It crosses the equator at 13:30 local time on an

196 ascending node. To cover the GEMS observation area, we used CALIOP data of 3-4

197 orbits per day. For the vertical information, the resolution for vertical sampling is 30 m

198 below 8 km altitude, and 60 m from 8 to 20 km altitude, respectively. Although the

199 CALIOP retrieves the data with extremely high horizontal and vertical resolutions, the

200 spatial coverage is narrow because the footprint of the CALIOP is about 90 m at the

201 Earth surface. In this study, the data of Level 2 aerosol profile product (APro, version

202 3.41) was used (Tackett et al., 2018). The aerosol profile product simultaneously

203 includes both aerosol and cloud optical depth. In addition, extinction quality flag

204 (Extinction_QC_Flag) data shows the quality of extinction profile. In this study, we

205 checked and used the quality flag value at 532 nm for the aerosol extinction coefficient

206 profile data. The AOD from CALIOP is vertically integrated aerosol extinction

207 coefficient from surface to top of atmosphere, and representative layer height

208 parameters (ALH and AEH) are directly estimated by using the vertical profile of

209 aerosol extinction coefficient at 532 nm to minimize the spectral discrepancy of aerosol

210 extinction. For the ALH retrieval, we adopted mean extinction height from the CALIOP

211 extinction coefficient profile (e.g., Koffi et al., 2012; Xu et al., 2019). Similarly, the

212 AEH estimation from CALIOP is also used to the extinction coefficient profile.

213

214 **2.4 Data Selection and Colocation**

215 In this study, we used data within 75°E-145°E for east-west and 5°S-45°N for north-

216 south direction, which is the observation area of GEMS. From Park et al. (2020), the

217 spatial range of highly coincident AOD is 30-40 km. To ensure that the number of

218 retrieved observation pixels that can be analyzed in this study is sufficiently high, we

219 relax the spatial limits for colocation matching. For spatial colocation, we selected

220 pixels for which distance between GEMS and CALIOP (or TROPOMI) observations

221 was less than 50 km. In addition, only the closest 10% of pixels were used. Given the

222 different orbital characteristics of CALIOP (or TROPOMI) and GEMS, temporal

223 colocation was also considered. During the period of image scanning from east to west

224 over Asia by GEMS, CALIOP and TROPOMI pass through the GEMS observation area

225 from south to north every 98.3 minutes. On average, two low earth orbit (LEO)

226 satellites pass three to four orbits through the GEMS scan area during a single day of

227 daytime observation. To consider these different orbital characteristics, only

228 observations taken within ±1 hour of the GEMS observation time was selected for

229 temporal colocation. As GEMS observes hourly, colocated pixels between the two

230 satellites shift from east to west over time.

231 To ensure the accuracy of ALH from TROPOMI, only pixels with quality assurance

232 (QA) values of 1.0 were used. To minimize the cloud contamination, the TROPOMI

233 ALH product uses the VIIRS cloud mask information and cloud parameters from the

234 Fast Retrieval Scheme for Clouds from the Oxygen A-band (FRESCO). To consider the

235 cloud contamination for the aerosol products, in addition, the VIIRS cirrus cloud

236 reflectance (viirs_cirrus_reflectance < 0.4), VIIRS cloud mask (viirs_cloud_mask < 0.1),

237 and cloud fraction from the FRESCO (cloud_fraction < 0.1) are considered in this study

238 (Michailidis et al., 2023). However, de Graaf *et al.* (2022) showed that respective cloud

239 masking methods have difficulty detecting various clouds. For this reason, cloud

240 contamination remains a critical source of uncertainty in the ALH retrieval. From

241 previous studies, the UVAI is used to detect the presence of absorbing aerosol (e.g.,

242 Chen et al., 2021; Griffin et al., 2020; Michailidis et al., 2023; Sanders et al., 2015), and

243 the aerosol height information was only retrieved on the absorbing aerosol pixels.

244 However, the GEMS aerosol product is retrieved not only the absorbing aerosols, but

245 also the non-absorbing aerosols. For this reason, the pixels for which with an AOD at

246 443 nm (AOD_{443} hereafter) taken from the GEMS aerosol product exceed 0.3 are

247 selected for AEH retrieval.

248

249 **3. AEH retrieval algorithm**

250 AEH is a layer height parameter that considers the penetration of photons into the

251 aerosol layer. It is defined such that the integral of the vertical aerosol extinction profile

252 from the surface to the AEH is equal to $(1-e^{-1}) \times AOD$, as defined by Park *et al.* (2016).

253 Numerous previous studies have used the aerosol top layer height (Kohkanovsky and

254 Rozanov, 2010) or middle layer height (i.e. ALH or centroid height) (e.g., Sanders *et al.*,

255 2015; Nanda *et al.*, 2020) as the aerosol vertical layer parameter. AEH is similar to the

256 aerosol top layer height but with a slight bias.

257 For AEH retrieval, the vertical distribution assumption is also important. The

258 Gaussian Density Fitting (GDF) distribution, which is a modified Gaussian distribution

259   structure by considering the range of upper and lower boundary height, is assumed for

260   AEH retrieval. The full-width at half-maximum (FWHM) of the aerosol layer is

261   assumed to be 1 km. A schematic description of AEH and other aerosol vertical

262   parameters are shown in Figure 1. Based on the assumptions about the aerosol vertical

263   distribution, the AEH value is higher than the peak height of the Gaussian distribution

264   and lower than the aerosol top layer height. Otherwise, the ALH is defined as the

265   integral of the vertical aerosol extinction profile from the surface to the ALH is equal to

266   0.5 × AOD. This assumption is used by Nanda et al. (2016). Therefore, the ALH equals

267   the peak height of the profile in the conditions shown in Figure 1.

268
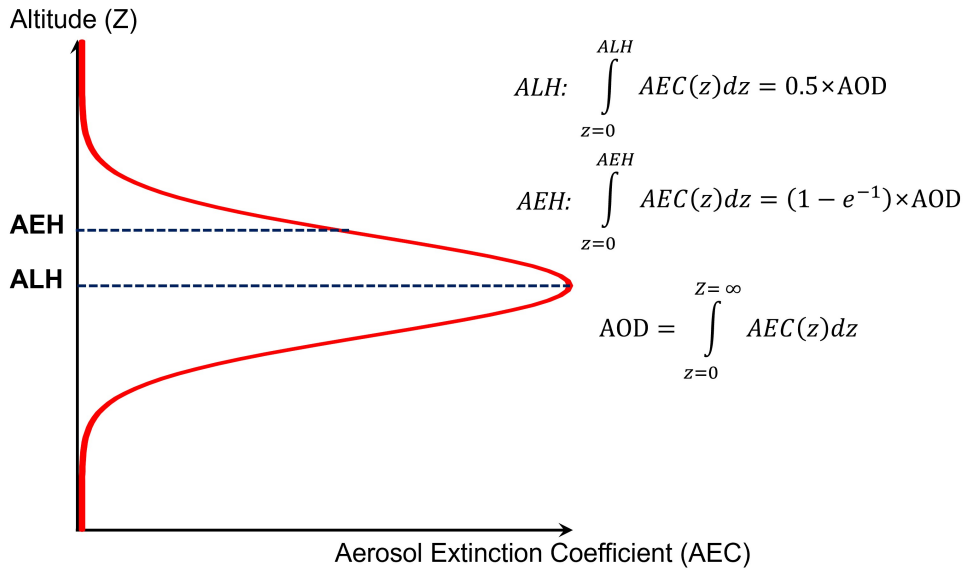
269   **Figure 1.** A schematic illustration of AEH and ALH definitions in an idealized

270   Gaussian shape of aerosol vertical distribution.
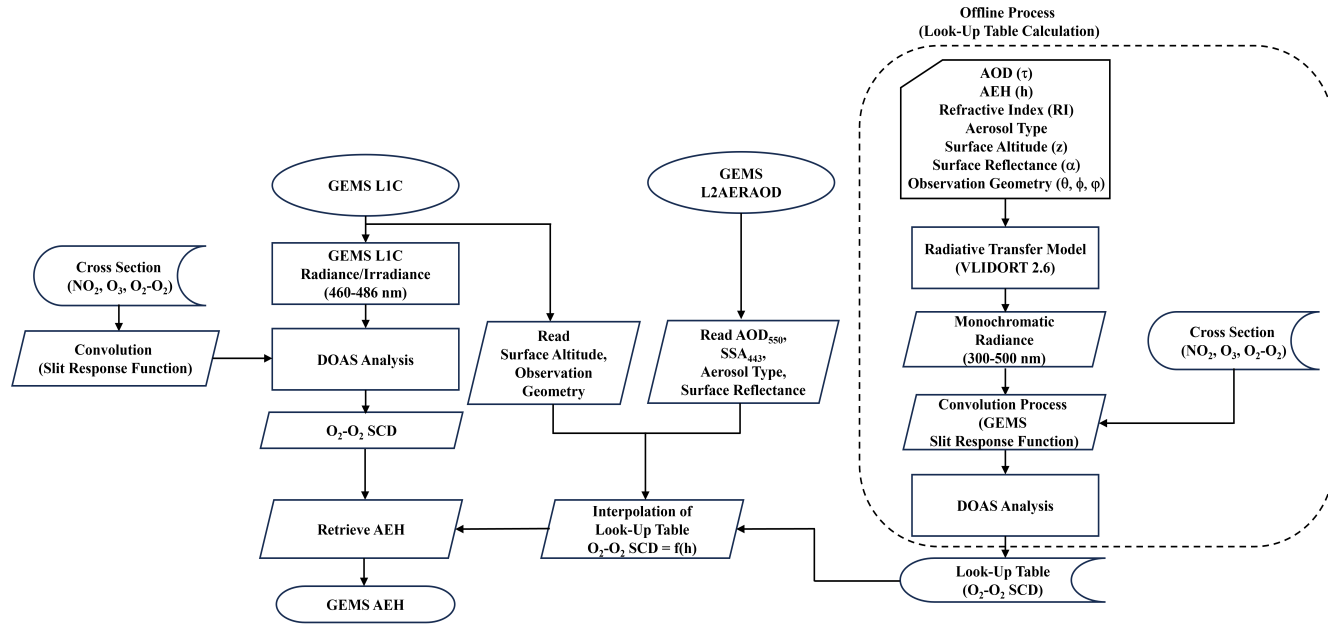
271
272 **Figure 2.** Flowchart of the AEH retrieval algorithm for GEMS satellite observation.

273

274 For AEH retrieval, the basic idea is the identification of changes in optical path length

275 caused by effective aerosol layer height variation. To measure the optical path length

276 change, O_2-O_2 SCD retrieved by the DOAS method was used because the spectral

277 coverage is limited to 300-500 nm (Park et al., 2016, Kim et al., 2020). In the GEMS

278 product, the O_2-O_2 SCD at 477 nm absorption band is the most useful absorption band

279 because this absorption band is strongest absorption band within the GEMS spectral

280 observation range. Figure 2 shows the overall flowchart of the AEH algorithm for

281 GEMS satellite. The AEH algorithm for GEMS employs a look-up table (LUT) that

282 contains O_2-O_2 slant column density (SCD) values for many scenarios with a variety of

283 observation geometries [solar zenith angle (SZA; θ), viewing zenith angle (VZA; Φ),

284 relative azimuth angle (RAA; φ)], surface altitude (z), surface reflectance (α), AOD (τ),

285 AEH (h), Refractive Index (RI) for SSA, and aerosol type. During the radiance

286 simulation, the radiance is monochromatically simulated and then convolved with the

287 GEMS instrument spectral response function. Finally, the radiance information is

288 converted to the O_2-O_2 SCD from differential optical absorption spectroscopy (DOAS)

289 method (Platt, 1994).

290 DOAS method has been frequently used to estimate the amount of trace gases (i.e.,

291 SCD of trace gas) from ground (e.g., Cheng et al., 2023; Irie et al., 2008; Platt and Stutz,

292 2008; Wagner et al., 2011; Wang et al., 2017) and satellite (e.g., Kwon et al., 2019; Li et

293 al., 2023; Wagner et al., 2007, 2010) measurements. Detailed DOAS fitting parameter

294 and setting information is provided in Table 1 for the estimation of O_2-O_2 SCD from

295 both the simulation and observation data. For the O_2-O_2 SCD estimation at 477 nm, the

296 fitting window ranges from 460 to 486 nm to cover the full absorption structure of O_2-

297 O_2. Within the fitting window, the absorptions of NO_2 and O_3 are significant. To

298 describe these two absorbing species, temperature dependent cross section information

299 is adopted. The temperature dependent cross section setting considers stratosphere and

300 troposphere, simultaneously.

301

302 **Table 1.** Details of fitting parameter for O_2-O_2 SCD estimation via the DOAS method.

Parameter	
Fitting window	460 – 486 nm
Absorption cross section	NO_2 at 220 and 294 K (Vandaele *et al.*, 1998)
	O_3 at 223, 243 and 293K (Bogumil *et al.*, 2001)
	O_2-O_2 at 293 K (Thalman and Volkamer, 2013)
	Ring

303

304

305 **Table 2.** Ratio between SCD error and the SCD of O_2-O_2 according to the polynomial

306 order and offset settings used for DOAS fitting.

Polynomial	Offset = none	Offset = 0th
2nd order	6.06 ± 2.07	6.79 ± 2.31
3rd order	6.32 ± 2.20	6.79 ± 2.32
4th order	7.86 ± 2.78	7.34 ± 2.85

307

308 To minimize the noise effect and improve DOAS fitting quality, the optimal settings

309 for fitting were also analyzed. Table 2 shows ratios of O_2-O_2 SCD error to the O_2-O_2

310 SCD for various polynomial and bias orders from observed radiance. The polynomial

311 and offset are basic fitting parameters for the DOAS fitting. Two parameters describe

312 the broadband spectral feature of radiance before identifying the gas absorption

313 structure. The ratio between SCD error and the SCD of O_2-O_2 is important to determine

314 the AEH retrieval quality. When the fitting error increases, the uncertainty of AEH is

315 also enhanced during the retrieval. Smallest AEH fitting errors are obtained by a DOAS

316 fit with a 2nd order of polynomial, and 'none' offset. These settings are used in the

317 GEMS AEH algorithm.

318 In estimating AEH, other aerosol characteristics, including AOD and aerosol optical

319 properties, affect retrieval accuracy. Park et al. (2016) have shown that the largest

320 contributor to the AEH uncertainty is associated with the uncertainty in SSA. In

321 addition, the AEH retrieval uncertainty due to error in the aerosol optical properties (e.g.,

322 AOD and phase function) and surface reflectance has dependence on observation

323 geometries. After the estimation of O_2-O_2 SCD, for this reason, conversion from O_2-O_2

324   SCD to AEH is an essential process. Table 3 shows dimensions of the LUT for the AEH

325   retrieval algorithm. To calculate the LUT, a linearized pseudo-spherical vector discrete

326   ordinate radiative transfer model (VLIDORT) version 2.6 was used (Spurr, 2013).

327   During the radiative transfer model simulation, reference wavelength for the SSA and

328   AOD is assumed to be 440 nm. The aerosol type is defined by the radiative absorptivity

329   and particle size information. The aerosol type is classified as absorbing, dust, and non-

330   absorbing aerosol. Absorbing and non-absorbing aerosol types are assumed to be the

331   fine-mode dominant particles. For the spectral conversion of AOD, the angstrom

332   exponents of 1.186, 0.222, and 1.179 are used for absorbing, dust, and non-absorbing

333   aerosol, respectively. The SSA is assumed to be spectrally constant within the spectral

334   range for O_2-O_2 estimation. Although the spectral O_2-O_2 absorption band is around 477

335   nm, the spectral discrepancy between reference wavelength for aerosol optical

336   properties and center wavelength of O_2-O_2 absorption is assumed to be ignored in this

337   study. After calculating spectral radiance with 0.1 nm sampling, the convolution with

338   the GEMS slit response function was applied, and the spectra were sampled on the

339   spectral grid of the GEMS radiance data (Level 1C) prior to the DOAS fitting. Radiative

340   transfer calculations were performed accounting for the temperature dependence of

341   absorption cross section for O_2-O_2 (e.g., Park *et al.*, 2017).

342

343

344

345

346

347

348   **Table 3.** The dimension of the LUT for the GEMS AEH retrieval algorithm used to

349   estimate AEH from O_2-O_2 SCD. (SZA: solar zenith angle, VZA: viewing zenith angle,

350   RAA: relative azimuth angle, SUR: surface reflectance).

Variable [unit]	No. of entries	Entries	
Spectral range [nm]	-	455-491 nm (0.1 nm interval)	
SZA [º]	7	0.01, 10, 20, 30, 40, 50, 60	
VZA [o]	7	0.01, 10, 20, 30, 40, 50, 60	
RAA [o]	10	0.01,20, 40, 60, 80, 100, 120, 140, 160, 180	
SUR	3	0.0, 0.05, 0.2	
AOD at 440 nm	11	0.04, 0.2, 0.4, 0.7, 1.0, 1.3, 1.6, 2.0, 2.5, 3.0, 5.0	
Refractive Index (Imaginary) at 440 nm	3×3	**Absorbing** (Real: 1.45)	0.000, 0.0074, 0.0314
		Dust (Real: 1.53)	0.0, 0.0030, 0.0080
		Non-Absorbing (Real: 1.41)	0.0, 0.0040, 0.0156
AEH [km]	13	0.0 (Extrapolate), 0.2, 0.5, 1.0, 1.3,1.6, 2.0, 2.3, 2.7, 3.0, 3.5, 5.0, 10.0 (Extrapolate)	
Terrain Height [km]	2	0.0, 2.0	
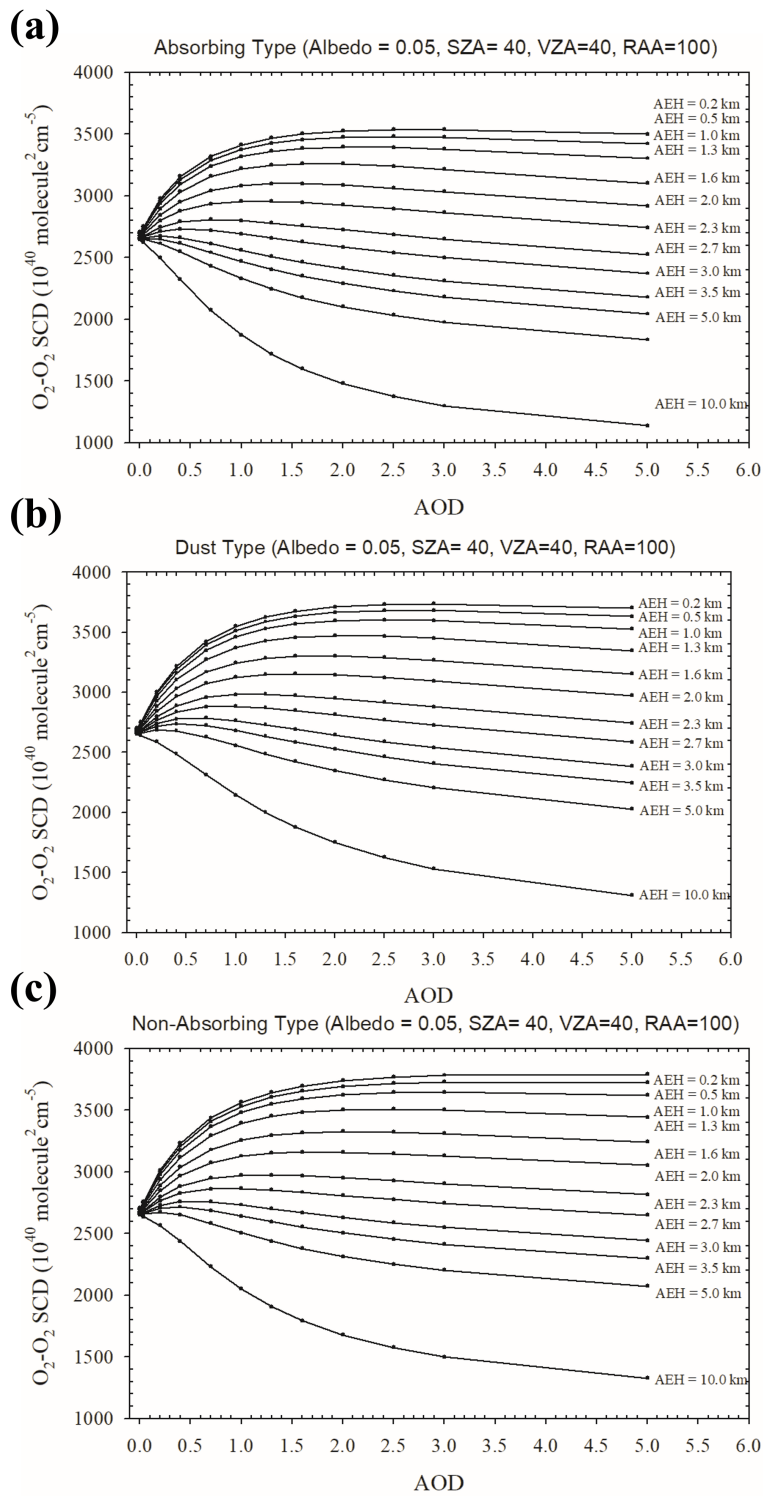
Figure 3. O_2-O_2 SCD dependence as a function of AOD and AEH for (a) Absorbing,

(b) Dust, and (c) Non-Absorbing aerosol types.

355   Figure 3 shows the example of O_2-O_2 SCD dependence as a function of AOD and

356   AEH from the LUT according to the respective aerosol types and AOD. O_2-O_2 SCD

357   decreases with increasing AEH for all aerosol types and AOD (Park *et al.*, 2016).

358   Similar to the previous study, the O_2-O_2 SCD sensitivity is enhanced at high AOD and

359   absorbing aerosol cases from GEMS LUT. In addition, the contrast of O_2-O_2 SCD is

360   greater for absorbing aerosols than non-absorbing aerosols. During the radiance passing

361   through the aerosol layer, the absorbing aerosol is more efficiently absorbed the

362   radiance. For this reason, the effective optical path length is significantly shorter for

363   absorbing aerosols.

364   The AEH algorithm used the GEMS operational AOD and surface reflectance.

365   However, those retrieval results include the uncertainties. Figure 4 shows the AEH

366   retrieval uncertainty based on the O_2-O_2 SCD LUT with an AOD error of 0.2. The

367   retrieval uncertainty of AEH was evaluated as the relative ratio of SCD changes with

368   respect to input variables. This ratio is defined by the relationship between changes in

369   SCD per unit AEH and changes in SCD due to uncertainties in input variables. The

370   AOD error of 0.2 is twice the target accuracy of the GEMS standard algorithm product.

371   Because the O_2-O_2 SCD change is small in high AOD, the AEH retrieval uncertainty is

372   relatively small in high AOD condition. In addition, the SCD sensitivity in high AEH is

373   weak due to the vertical distribution characteristics of O_2-O_2. Thus, the AEH uncertainty

374   is up to 0.9 km at high AEH case in moderate AOD cases (around 0.5-1.0).

375   Figure 5 shows the AEH retrieval uncertainty with the surface reflectance error of

376   0.02. Because surface reflection and aerosol scattering simultaneously affect the

377   increase in optical path length, surface reflectance uncertainty has a significant impact

378   especially to low AOD. The AEH retrieval error due to uncertainty in surface

379 reflectance is larger than 1 km in cases with AOD < 0.4. In addition, the AEH error by

380 the surface reflectance uncertainty linearly decreases with increasing AOD, indicating

381 relatively small impact with aerosol height change.
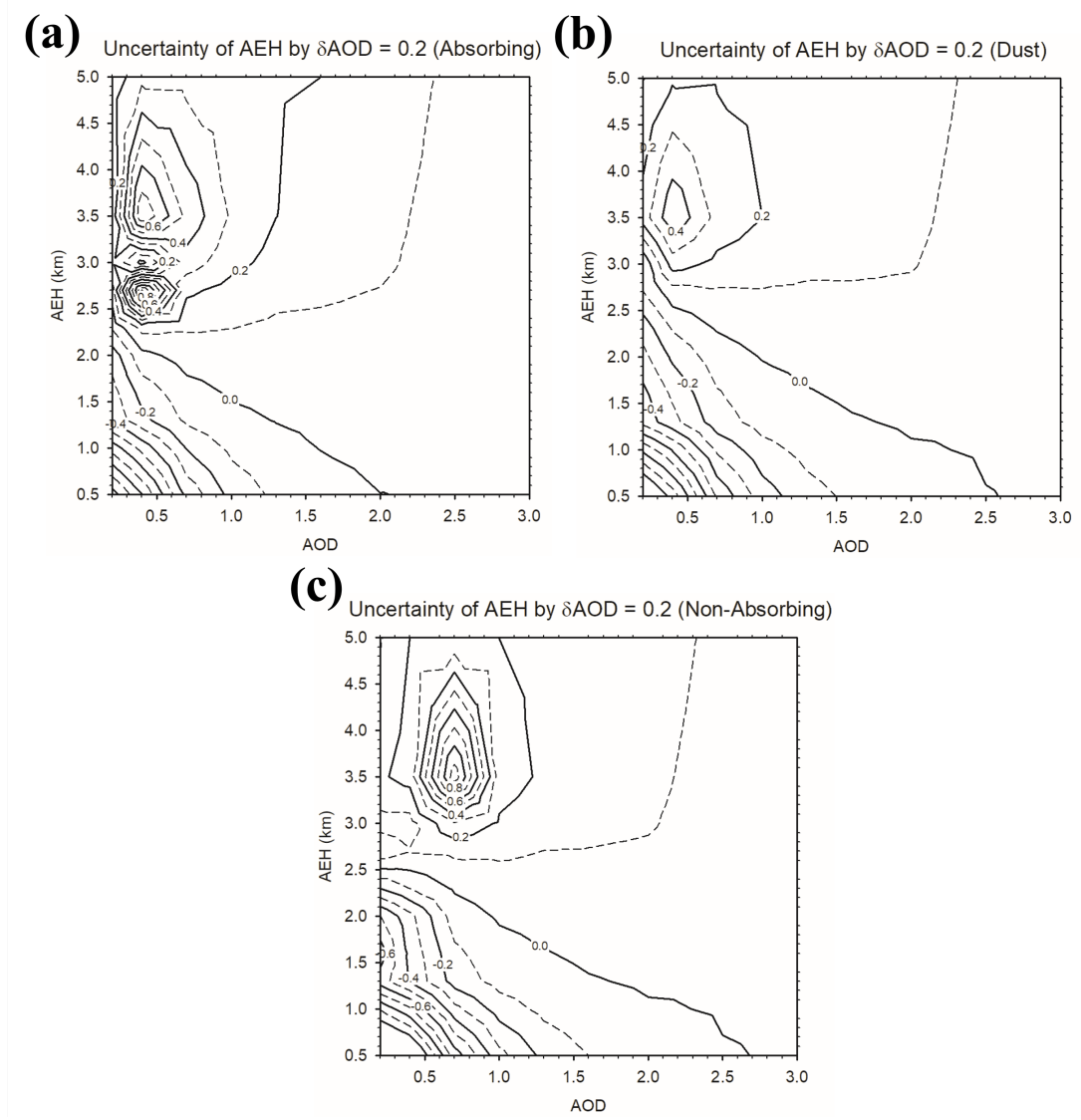
382

383 **Figure 4.** AEH retrieval uncertainty due to the AOD error of 0.2 for cases with (a)

384 Absorbing, (b) Dust, and (c) Non-Absorbing aerosol types.

385
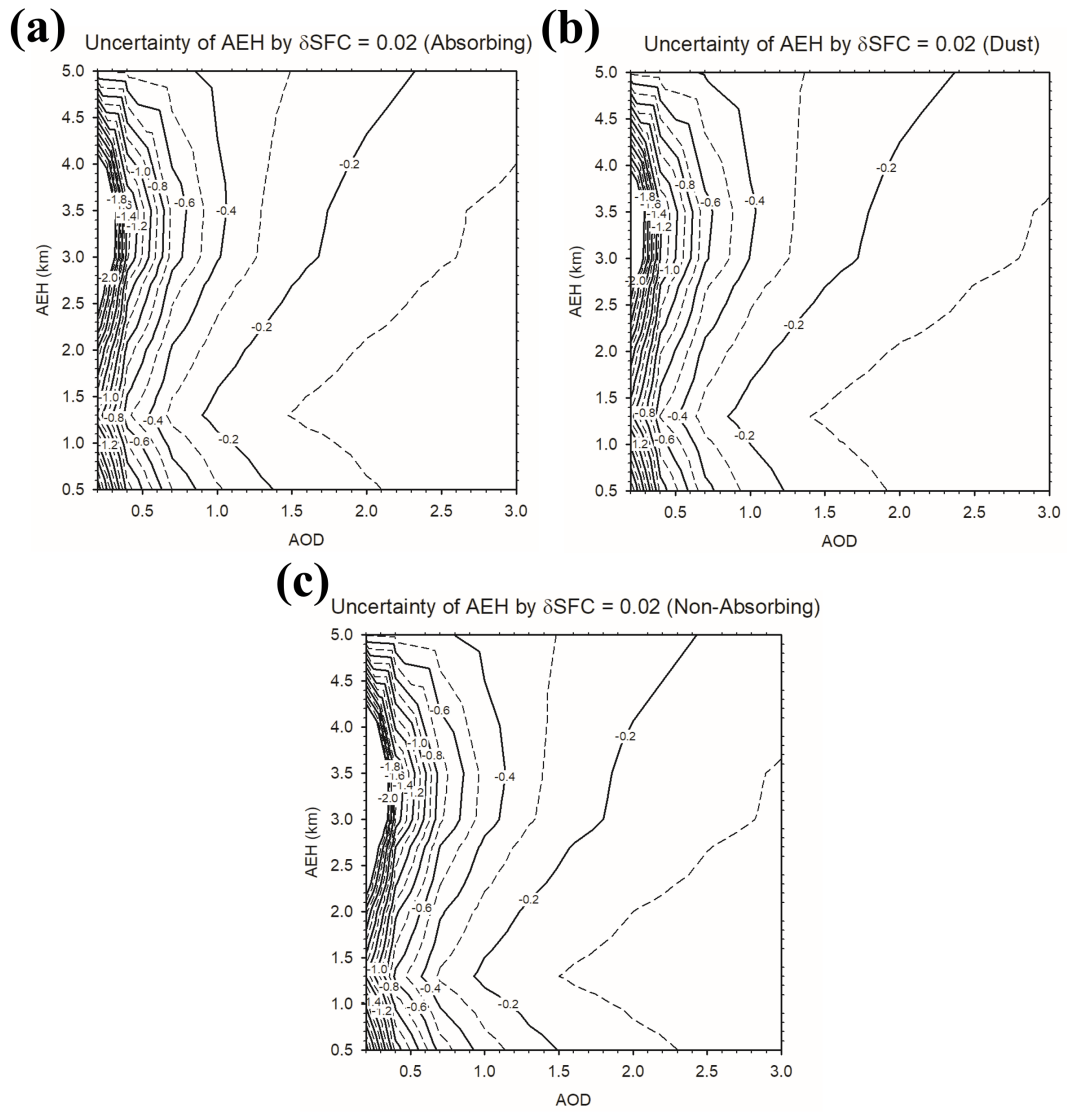
Figure 5. AEH retrieval uncertainty due to the surface reflectance error of 0.02 for
cases with (a) Absorbing, (b) Dust, and (c) Non-Absorbing aerosol types.

388

389
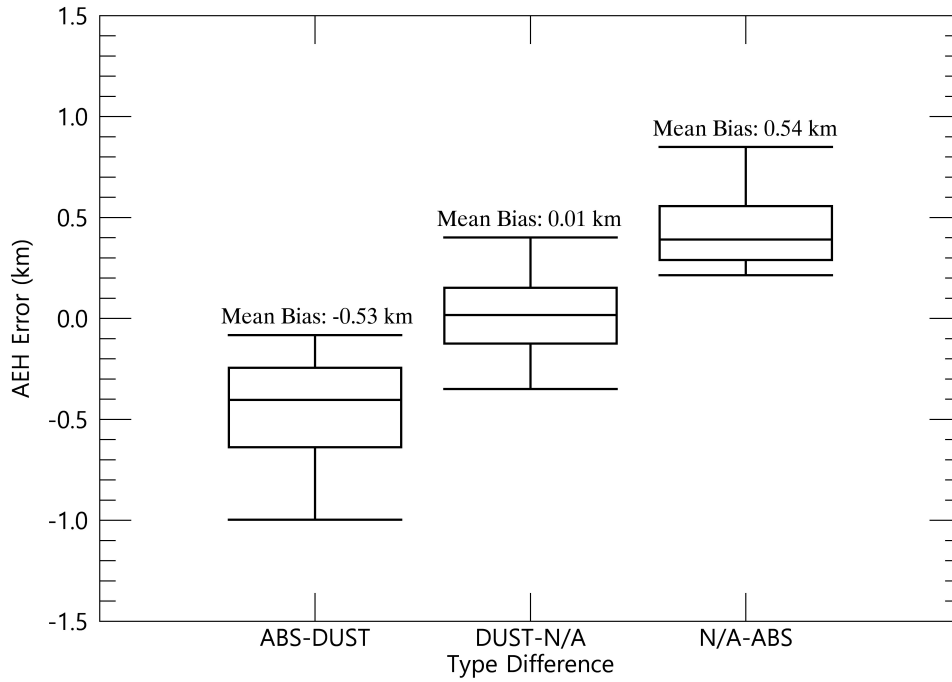
Figure 6. AEH retrieval uncertainty caused by the aerosol type misclassification.

391

Figure 6 shows the retrieval uncertainty caused by misclassification of the aerosol types. On average, the AEH retrieval uncertainty takes values up to 0.5 km, but this uncertainty shows larger than 2 km under low AOD and short optical path length conditions. From the sensitivity analysis, aerosol type (in terms of SSA) and AOD, and surface reflectance are carefully considered as input parameters for AEH retrieval.

In the AEH retrieval, the AOD, aerosol type, and SSA are obtained from the L2AERAOD, which is standard aerosol product of GEMS. The aerosol vertical distribution is always fixed as GDF function profiles as shown in Spurr and Christi (2014).

401

402

4. Case studies

Figure 7 shows retrieval results for AEH from GEMS on March 29 over East Asia. Because the operational schedule is hourly during the daytime, the GEMS retrieval results are shown at 1-hour intervals from 01:00 to 07:00 Universal Time Coordinated (UTC). AOD_{443} and SSA at 443 nm (SSA_{443} hereafter) are also shown in Figures S1 and S2, respectively. Pixels with low AOD_{443} values have large AEH uncertainty due to weak aerosol scattering information (see also Park *et al.*, 2016). For this reason, only AEH retrieval results with AOD greater than 0.3 are shown in this study. In addition, the AEH retrieval results are only shown to the "Reliable" quality flag of L2AERAOD, which is estimated to the aerosol optical properties with significant averaging kernel for optimal estimation in L2AERAOD. A case was analyzed in which a dust plume was located along the coast of China and South Korea with AOD_{443} of 0.8-1.2. Simultaneously, another plume was also present over the northeastern Korean Peninsula with AOD_{443} of 1.0-2.0. SSA_{443} was 0.90-0.93 for the plume over South Korea and 0.87-0.90 for the plume over the northeastern Korean Peninsula. Retrieved AEH results from these different plumes show similar ranges. For both detected plumes, the AEH shows similar patterns and takes values ranging between 1.0 and 2.0 km in this case.
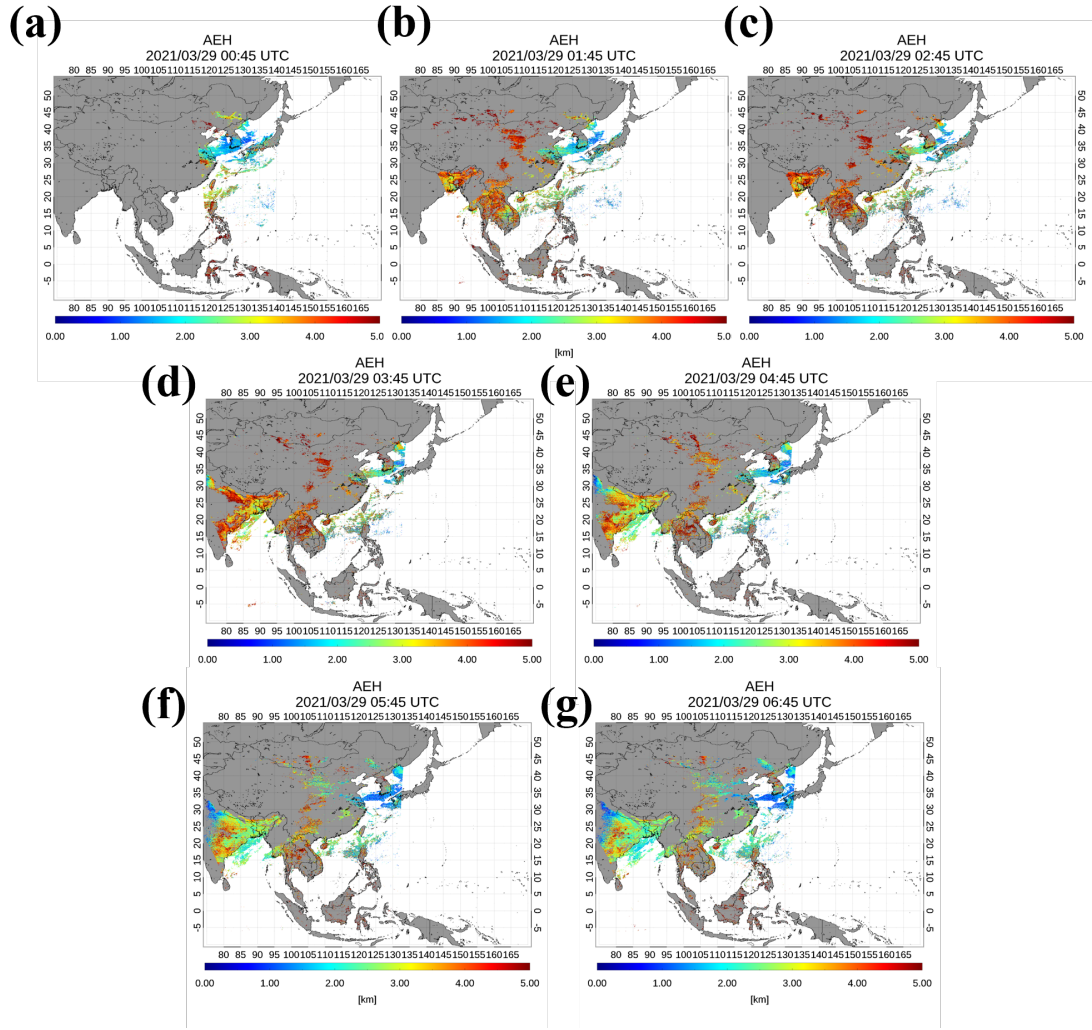
Figure 7. Case study results for AEH based on GEMS observations on March 29, 2021 [(a) 00:45 UTC, (b) 01:45 UTC, (c) 02:45 UTC, (d) 03:45 UTC, (e) 04:45 UTC, (f) 05:45 UTC, and (g) 06:45 UTC].

An additional severe aerosol plume was present over northeastern India, with AOD_{443} of 1.0-2.0 and SSA_{443} of 0.85-0.90. According to Rana *et al.* (2019), metropolitan cities and industrial clusters in India are heavy emitters of black carbon, and high concentrations of black carbon are distributed over the Indo-Gangetic Plain (IGP). Therefore, the aerosol plume with high AOD and low SSA (high absorbing) is

430 considered a physical rather than an artifact due to edge of GEMS observation field.

431 Except for the inland parts of India, AEH in high AOD pixels ranged from 1.5 to 3.5 km.

(a) TROPOMI ALH 2021/03/28   **(b)** TROPOMI ALH 2021/03/29

432
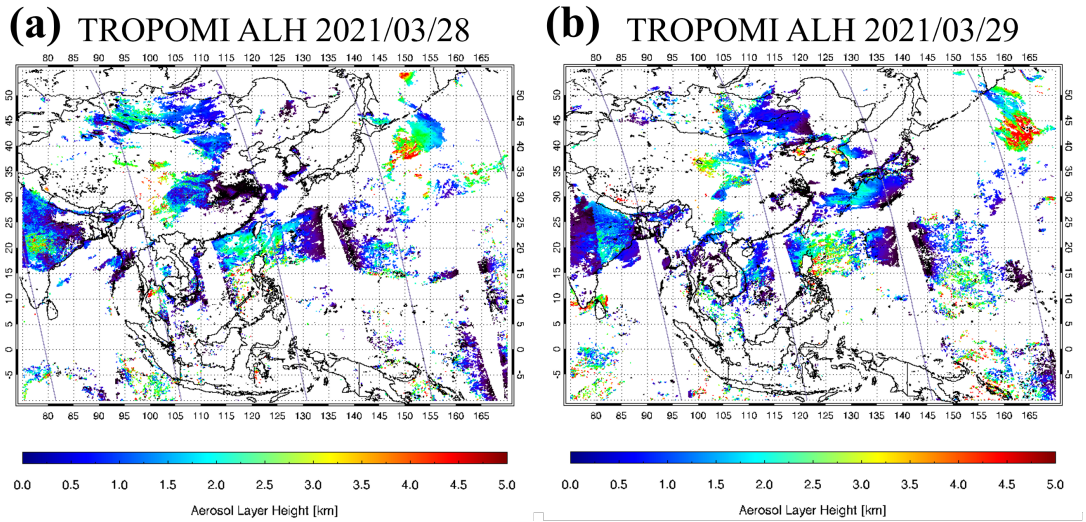
433 **Figure 8.** ALH retrieved from TROPOMI and orbit path of CALIOP on (a) March 28

434 and (b) March 29, 2021 (Unit: km).

435

436 For comparison of the retrieval, Figure 8 shows the ALH retrieved from TROPOMI

437 on March 28 and 29, 2021 over East Asia. A dust plume was transported from China to

438 South Korea during this period, then split into two distinct plumes over northeastern

439 China and the coastal area of South Korea. The ALH retrieved from TROPOMI for both

440 plumes range between 0.5 and 1.5 km. Given the difference in definition for the aerosol

441 height parameters between ALH and AEH as shown in Fig. 1, AEH values retrieved

442 from GEMS were higher than the ALH values retrieved from TROPOMI. In an ideal

443 case under symmetric gaussian distribution with a width of 1 km, the AEH from GEMS

444 was around 0.5 km higher than the peak height of aerosol layer. The ALH expresses the

445 center (or peak) height, thus, the AEH from GEMS was overestimated by around 0.5 km

446 relative to the ALH from TROPOMI. Although AEH had higher values than ALH from

447 TROPOMI, the GEMS AEH retrieval provided meaningful physical results for the dust

448 transport case study.

449
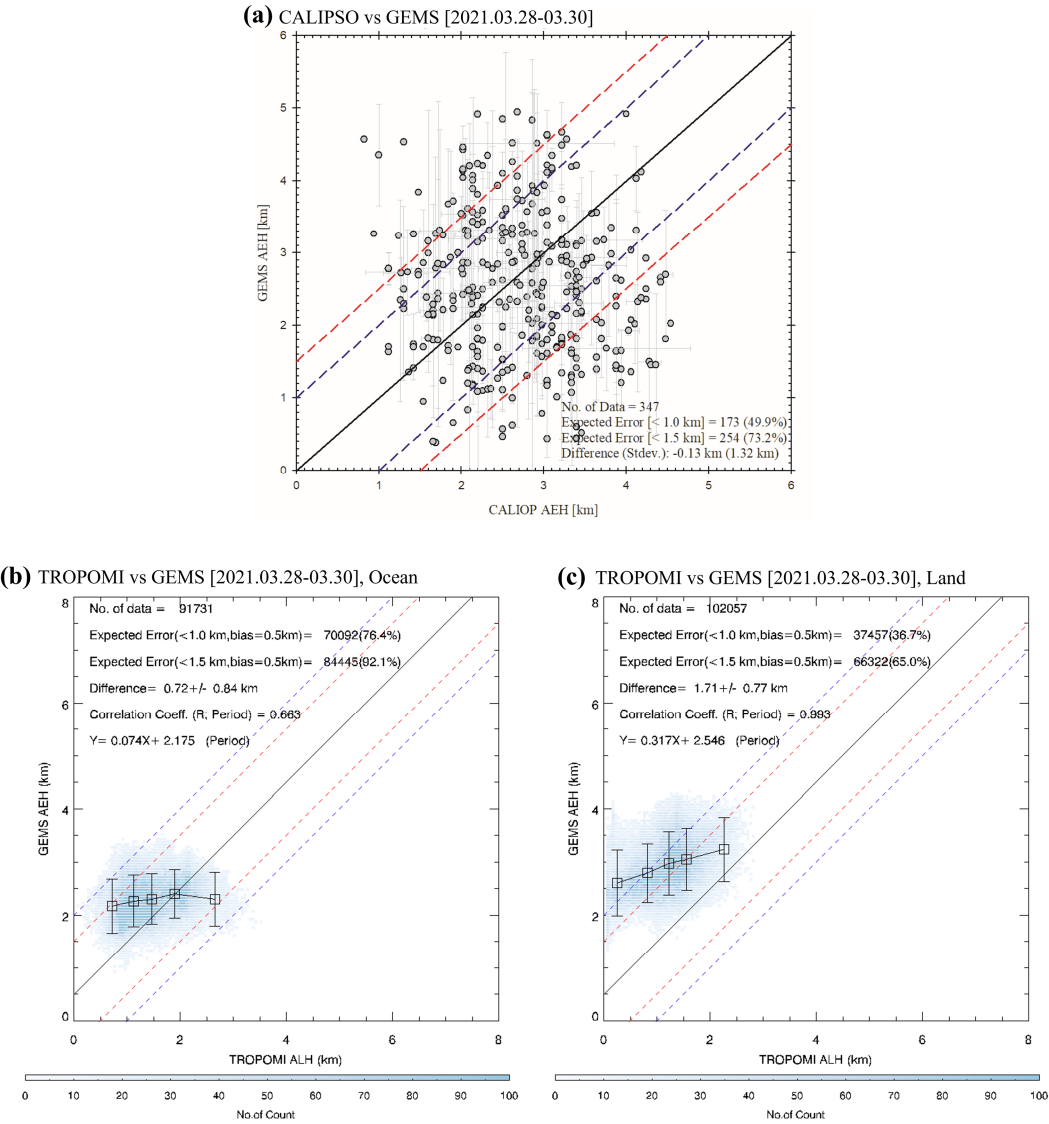
450 **Figure 9.** Intercomparison of (a) AEH between CALIOP and GEMS and (b) ALH

451 from TROPOMI and AEH from GEMS over ocean and (c) over land (Black box and

452 error bar is mean and standard deviation in 20% interval of each TROPOMI ALH) over

453 the period from March 28 to 30, 2021.

454

455 Figure 9 shows intercomparison results for aerosol plume height among GEMS,

456   CALIOP, and TROPOMI during the case study of dust transport in East Asia from

457   March 28 to 30, 2021. For the direct comparison shown in Figure 9a, the difference in

458   AEH between GEMS and CALIOP was -0.13±1.32 km. Nanda *et al.* (2020) reported

459   that the difference in ALH between TROPOMI and CALIOP was 0.53 km for 4 cases of

460   thick Saharan dust plumes. Large AEH uncertainty occurred mostly over the inland area

461   of China. Because AEH from GEMS uses only the O_2-O_2 absorption band, the accuracy

462   of AEH is sensitive to uncertainty in surface reflectance and AOD. From Park et al.

463   (2016), total error budget of AEH is 0.74-1.28 km, and the total error budget considered

464   the uncertainty of AOD, SSA, aerosol particle size, and surface reflectance in the

465   aerosol retrieval process. The total error budget amount from the previous study is

466   similar value of standard deviation of AEH difference between GEMS and CALIOP.

467   Figures 9b and 9c illustrate the comparison results between GEMS AEH and

468   TROPOMI ALH, for the period of March 28-30, 2021, over land and ocean surface,

469   respectively. The difference between GEMS AEH and TROPOMI ALH was 0.72 ± 0.84

470   km and 1.71 ± 0.77 km over ocean and land in this case, respectively. In addition, 82.4%

471   and 37.3% of all pixels had differences of less than 1.5 km over ocean and land,

472   respectively. However, the ALH from TROPOMI is generally lower than the AEH from

473   GEMS because of the discrepancy in definitions. Based on the assumption of aerosol

474   vertical distribution for AEH retrieval, the difference between AEH and center height of

475   aerosol extinction profile is around 0.5 km. To consider the inconsistency of definition

476   between ALH and AEH, the difference between two retrieval results decreased to 0.5

477   km bias. After consideration of definition inconsistency, the proportion of pixels within

478   the expected error ranges of 1.5 km are enhanced to 92.1% and 65.0% over ocean and

479   land, respectively.

480
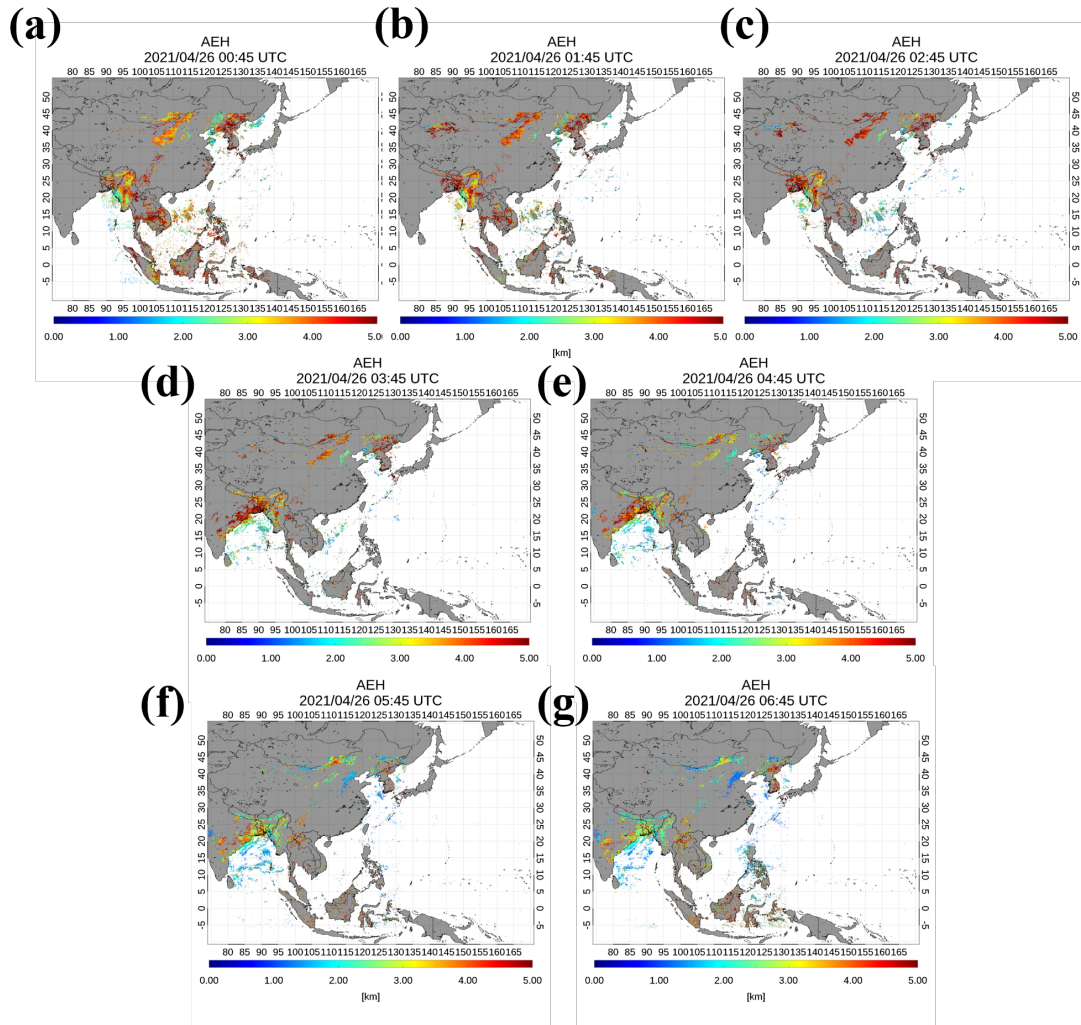
Figure 10. Case study results for AEH based on GEMS observations on April 26, 2021 [(a) 00:45 UTC, (b) 01:45 UTC, (c) 02:45 UTC, (d) 03:45 UTC, (e) 04:45 UTC, (f) 05:45 UTC, and (g) 06:45 UTC].

TROPOMI ALH 2021/04/26

484
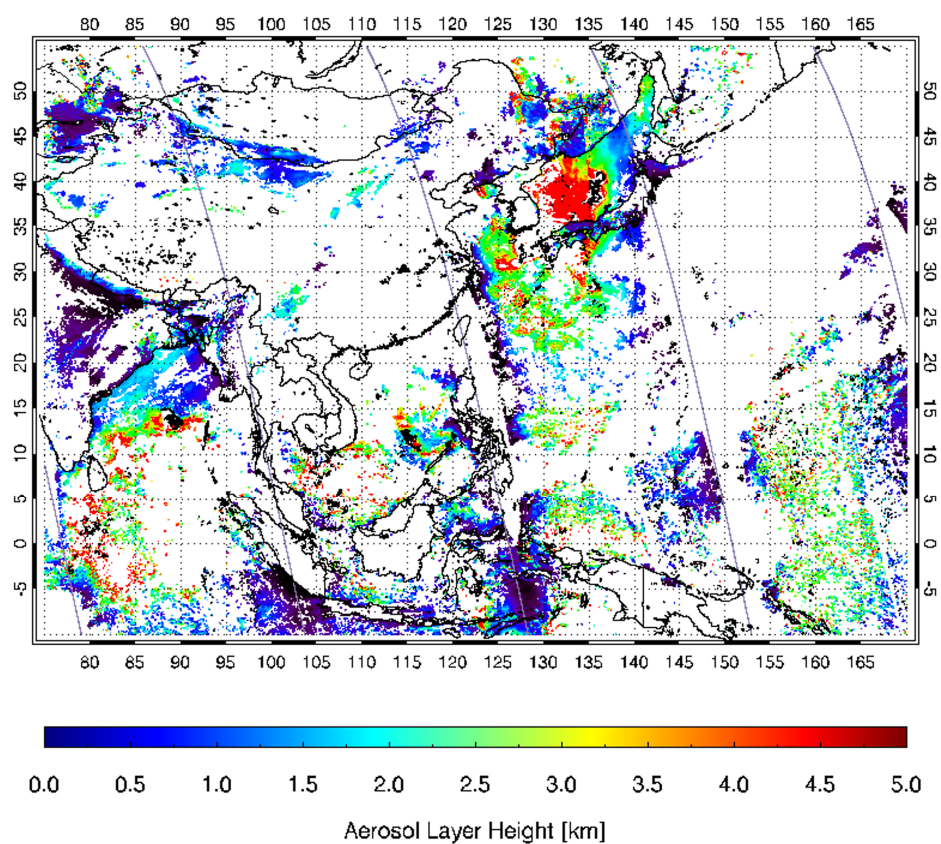
485   **Figure 11.** ALH retrieved from TROPOMI and orbit path of CALIOP on April 26,

486   2021 (Unit: km).
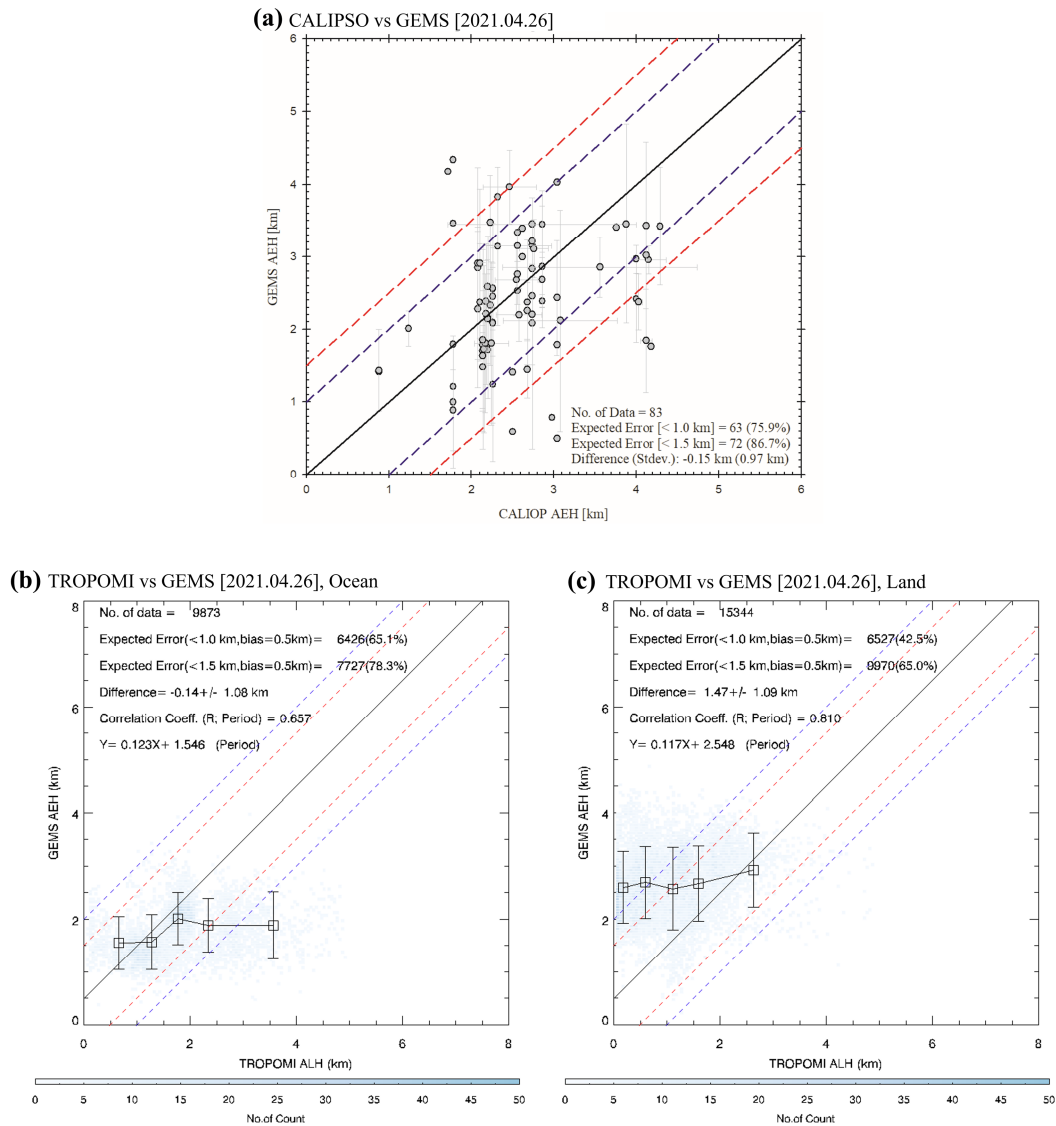
Figure 12. Intercomparison of (a) AEH between CALIOP and GEMS, and (b) ALH from TROPOMI and AEH from GEMS over ocean and (c) over land (black dot and error bar is mean and standard deviation in 20% interval of each TROPOMI ALH) on April 26, 2021.

An additional intercomparison case of April 26, 2021, is shown in Figures 10 (GEMS) and 11 (TROPOMI). During the transport of the dust plume from inland China to the coastal area, AEH changed from 4.0 km at 02:00 UTC to 2.0 km at 06:00 UTC.

496   By contrast, ALH from TROPOMI only observed the 1.5-2.5 km layer height over East

497   Asia around 04:00 UTC. Although the AEH from GEMS had spatio-temporal

498   uncertainty, this case demonstrates the advantage of AEH retrieval from GEMS for

499   continuous monitoring of changes in plume height during dust transport, in particular.

500   As shown in Figure 12, AEH from GEMS showed differences in height of -0.15 ± 0.97

501   km (compared to CALIOP). In addition, the differences in height of -0.14 ± 1.06 and

502   1.47 ± 1.09 km over ocean and land as compared to TROPOMI ALH.

503   From two different case results, proportion values within 1.0 km (or 1.5 km) height

504   difference between TROPOMI and GEMS have strong dependence of surface types.

505   The proportion over land (over ocean) was lower (higher) than the corresponding result

506   from the comparison of GEMS and CALIOP. The TROPOMI ALH from version 2

507   exhibits a strong surface type dependence as compared to the ground lidar data

508   (Michailidis et al., 2023). However, the relationship between TROPOMI ALH and

509   GEMS AEH in 20% interval of each TROPOMI ALH have high correlation coefficients.

510   In the case of March 28-30, the correlation coefficients between TROPOMI and GEMS

511   are 0.663 and 0.993 over ocean and land, respectively. In the case of April 26, the

512   correlation coefficients are 0.657 and 0.810 over ocean and land, respectively.

513

514   **5. Long-term validation**

515   For long-term validation, we used the AEH retrieval results from January to June,

516   2021. The CALIOP and TROPOMI satellites passed over the study area around 13:30

517   local time, which is around 04:30 UTC for East Asia and around 06:30 UTC for India.

518   Most temporal colocation pixels aligned with observation times of 04:00-06:00 UTC,

519   respectively. To check the dependence of several retrieval variables, the UVAI, AOD,

520 SSA, and dominant aerosol type in each pixel (TYPE) were obtained from the

521 L2AERAOD. Although the GEMS algorithm retrieved AEH in the range of 0-10 km,

522 the sensitivity of O_2-O_2 SCD to the optical path length was weak in cases of high AEH

523 because the vertical distribution of O_2-O_2 SCD is related to the square of the air

524 molecule densities. To ensure sufficient quality of retrieved data, therefore, the AEHs

525 from GEMS and CALIOP, and the ALH from TROPOMI were used only in pixels

526 where the AEH from GEMS were lower than 5 km.

527
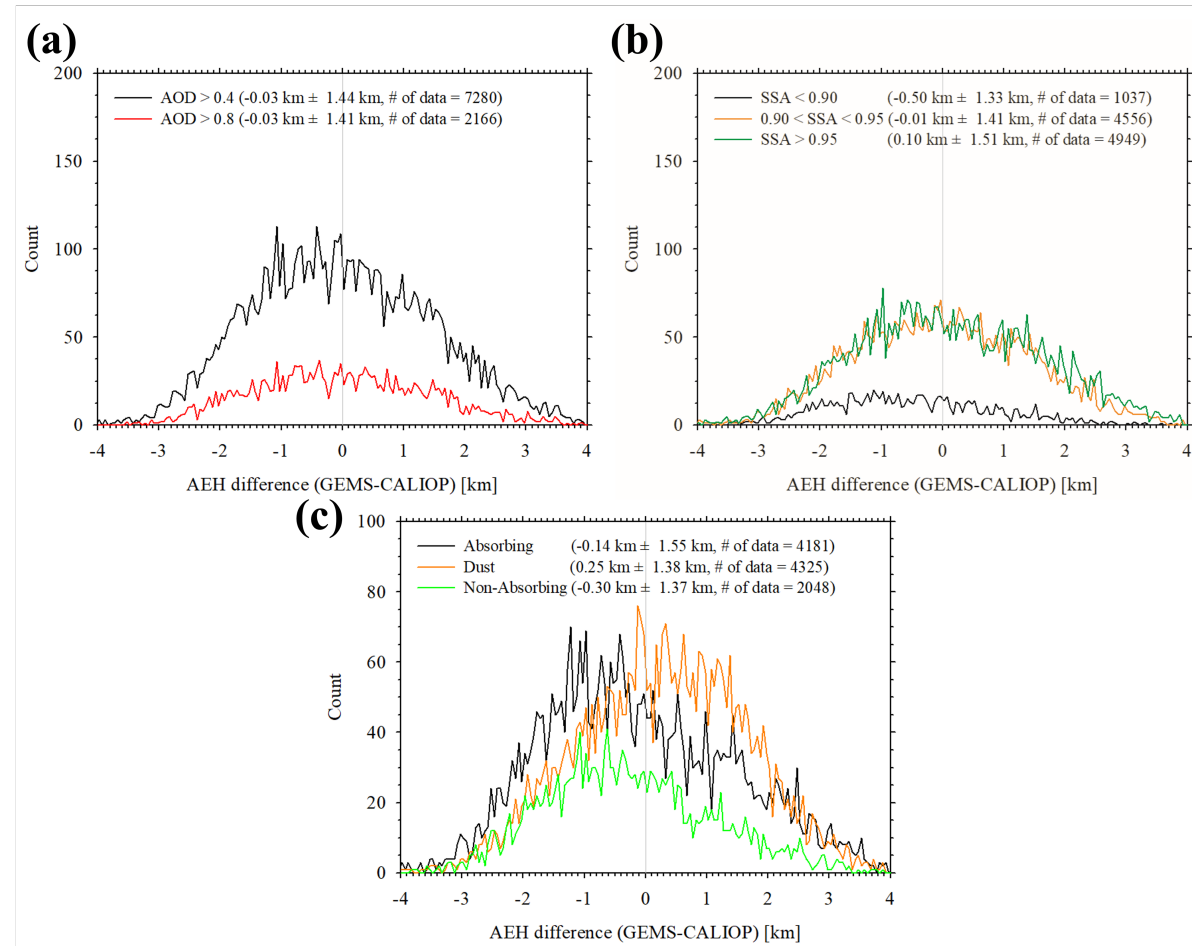
528 **Figure 13.** Histogram of AEH difference between CALIOP and GEMS with respect

529 to (a) AOD, (b) SSA, and (c) TYPE from GEMS over the period from January 1 to June

530 30, 2021.

531   Figure 13 shows histograms of difference in AEH between GEMS and CALIOP

532   according to AOD_{443}, SSA_{443}, and TYPE from GEMS. From Figure 13a, the

533   dependence on AOD threshold was insignificant; the average estimated AEH difference

534   was -0.03 km, but the variation in AEH difference was around 1.4 km based on the

535   standard deviation for $AOD_{443} > 0.4$. Because of uncertainty in GEMS aerosol

536   operational products, AEH from GEMS exhibits large variability. Although

537   L2AERAOD from GEMS retrieved the AOD, SSA, and aerosol types, the retrieved

538   results from L2AERAOD include significant uncertainty. Go et al. (2020) reported that

539   the root-mean square error (RMSE) of AOD between MODIS and OMI UV aerosol

540   algorithm is 0.276-0.341.

541   In addition, fitting error perturbs the fitting signals and tends to result in the

542   underestimation of SCD. Although the fitting error of O_2-O_2 SCD from GEMS radiance

543   was minimized, the fitting error has still remained around 6%, as indicated in Table 2.

544   The discrepancy in fitting condition between the simulated and observed radiance

545   biased the SCD estimation, which in turn led to bias and variation in the AEH retrieval.

546   Combined with the high sensitivity of AEH errors to aerosol optical properties,

547   uncertainty arising from L2AERAOD causes AEH variability.

548   The variation in AEH difference between observation platforms is shown in Figure

549   13b as a histogram according to SSA threshold. Across the entire SSA threshold range,

550   the standard deviation of the AEH difference was 1.33-1.51 km. In particular, this

551   standard deviation decreased slightly with decreasing SSA. The aerosol height

552   parameter is more sensitive to absorbing-dominant aerosols than scattering-dominant

553   aerosols (e.g., Park *et al.*, 2016; Nanda *et al.*, 2020). For this reason, the variability of

554   AEH is smaller in absorbing-dominant aerosols than scattering-dominant aerosols, if the

555   uncertainty of other aerosol parameters (AOD, SSA, and TYPE) is the same conditions.

556   Figure 13c shows the dependence of AEH difference on TYPE. The TYPE product

557   included dependence on the aerosol size and optical absorptivity. For this reason, the

558   AEH difference graphs for the "Dust" and "Absorbing" types differ, despite both types

559   being absorbing-dominant aerosols. The AEH difference for the "Absorbing" type

560   showed a negative bias with a large standard deviation, whereas a positive bias with a

561   small standard deviation was obtained for the "Dust" type. The AEH difference for the

562   "Non-Absorbing" aerosol type showed the largest negative bias in this comparison.

563   These results suggest that the aerosol size distribution of fine particles affects the

564   negative bias of AEH. Combined with the AEH difference bias illustrated in Figure 8b,

565   these findings indicate that the bias in AEH difference for "Absorbing" aerosols is

566   weakened by their absorbing-dominant property.

567   Figure 14 shows means and standard deviations for AEH difference between

568   CALIOP and GEMS according to AOD and AI values from GEMS. For AOD, the mean

569   AEH difference ranged from -0.13 to 0.03 km with a standard deviation of

570   approximately 1.45 km. Similar to Figure 13a, the variation in AEH difference with

571   AOD change was insignificant. For the AI, the lowest AEH difference was -0.19 km,

572   obtained for the AI range of 1.5-2.0. The largest AEH difference was 0.24 km for the AI

573   range of 4.0-4.5. Although the AEH difference varied slightly, no consistent tendency in

574   AEH variation with AI was observed. Overall, the standard deviation of AEH difference

575   ranged from 1.49 km (0.0 < AI < 0.5) to 1.18 km (4.5 < AI < 5.0), and a consistent

576   tendency of decreasing variance in AEH difference was found with increasing AI.

577
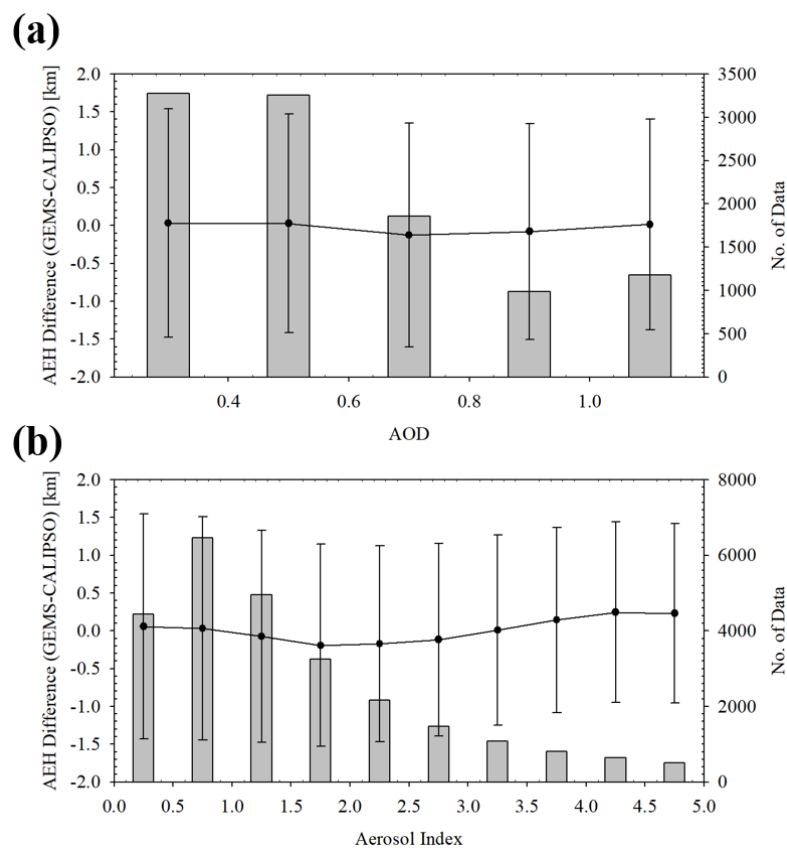
Figure 14. AEH difference between CALIOP and GEMS with respect to ranges of (a)

AOD and (b) AI obtained from GEMS from January 1 to June 30, 2021 (Black dots and

error bars denote the mean and standard deviation of AEH difference, while the gray-

box indicates the number of data).

582

583
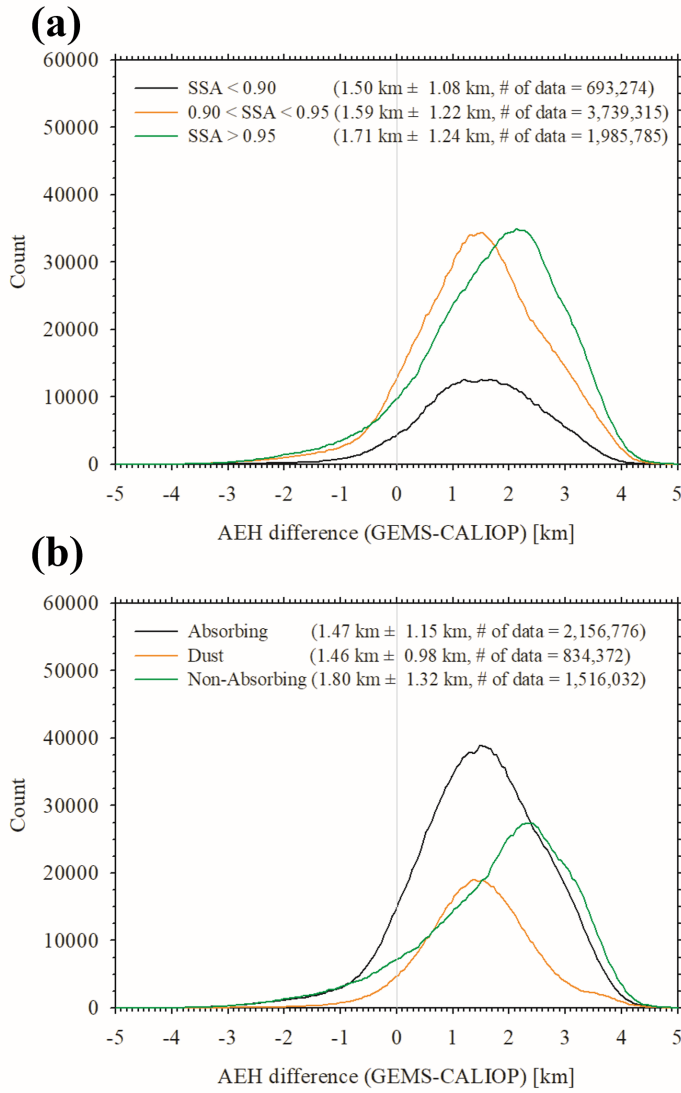
Figure 15. Histograms of differences between TROPOMI ALH and GEMS AEH with respect to (a) SSA, and (b) TYPE from GEMS in the period from January 1 to June 30, 2021.

587

588   Figure 15 shows histograms of differences between GEMS AEH and TROPOMI

589   ALH according to the SSA_{443} and TYPE obtained from GEMS. The difference between

590   GEMS AEH and TROPOMI ALH depends on both SSA and TYPE. The mean

591   difference value between GEMS AEH and TROPOMI ALH decreased as the aerosol

592   absorptivity increased. This difference was 1.50 ± 1.08, 1.59 ± 1.22, and 1.71 ± 1.24 km

593   for pixels of $SSA_{443} < 0.90$, $0.90 < SSA_{443} < 0.95$, and $SSA_{443} > 0.95$, respectively.

594   Comparing these results to Figure 13b, we find that the standard deviation of the

595   comparison with TROPOMI was approximately 75% of the corresponding value for

596   CALIOP. It is because both TROPOMI and GEMS are passive sensors that use similar

597   retrieval methods for oxygen absorption bands. Nanda *et al.* (2020) showed that the

598   operational algorithm of TROPOMI operational algorithm can provide ALH pixel

599   retrievals only for scenes dominated by absorbing aerosol particles. In addition, Griffin

600   *et al.* (2020) reported that the pixels with low positive UVAI values (weak absorbing

601   cases) are identified with low QA values ($QA \leq 0.5$) in the offline product of ALH.

602   Although the TROPOMI ALH algorithm updated for the expansion of retrieval range,

603   the contrast of O_2-O_2 SCD to the aerosol layer height change is fundamentally weak

604   sensitivity in scattering dominant aerosols (e.g., Park et al., 2016). For this reason, the

605   bias and standard deviation of height difference between GEMS and ALH is generally

606   larger in high SSA.

607   In addition, the difference between GEMS AEH and TROPOMI ALH depends on

608   TYPE, as shown in Figure 15b. The difference was 1.47 ± 1.15, 1.46 ± 0.98, and $1.80 \pm$

609   1.32 km for "Absorbing", "Dust", and "Non-Absorbing" type aerosols, respectively.

610   Similar to Figure 13c, the TYPE dependence of aerosol height information was

611   influenced by both absorptivity and size information. "Dust" type of aerosol is mainly

612   transported in the free troposphere with gaussian-like vertical distribution, and the

613   associated plume thickness is highly variable. However, "Absorbing" aerosols mainly

614   originate from anthropogenic emissions in East Asia and mostly distributed near the

615   surface with homogeneous concentration (e.g., Gao *et al.*, 2014; Wang *et al.*, 2012;

616 Peng *et al.*, 2016). Transport patterns and vertical distribution shape depending on

617 aerosol types, can affect the accuracy of aerosol height retrieval results.

618
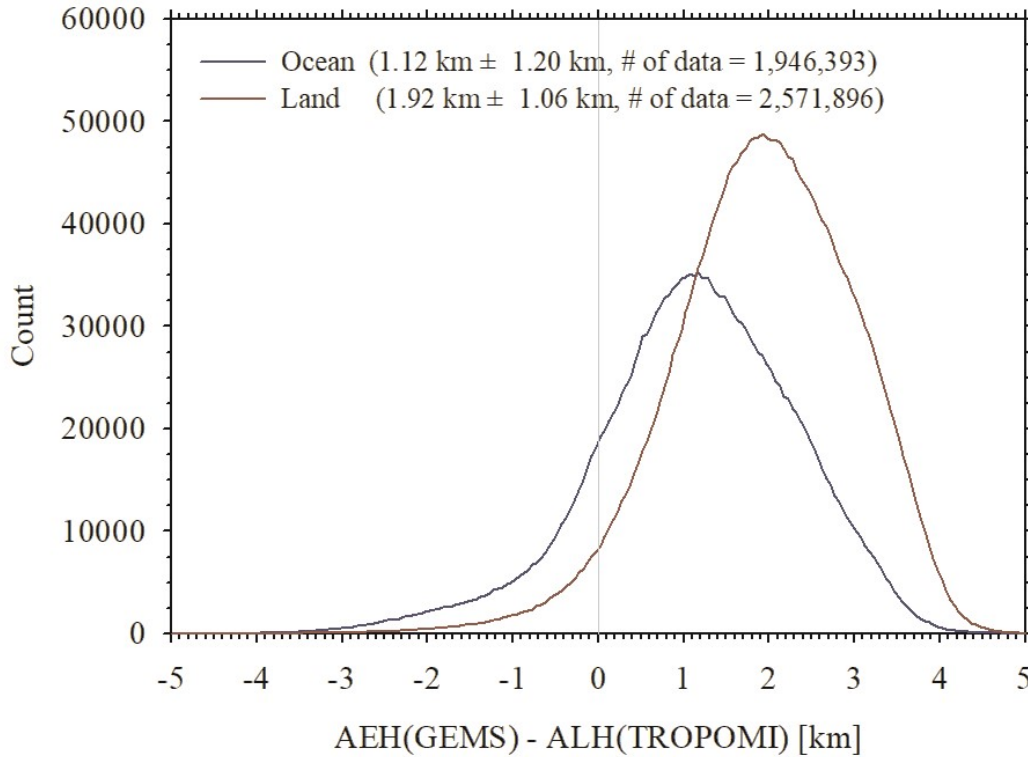
619 **Figure 16.** Histogram of the difference between TROPOMI ALH and GEMS AEH

620 over land and ocean pixels, respectively, from January 1 to June 30, 2021.

621

622 The non-Lambertian effect on the land surface impacted surface reflectance

623 uncertainty during AEH retrieval, and this effect led to bias and variance in AEH. In this

624 study, the minimum Lambertian equivalent reflectance was used as the reference

625 reflectance value. However, surface reflectivity has geometric dependence due to non-

626 Lambertian effects, which leads to a bias of 0.01-0.02 for surface reflectance over the

627 land surface (e.g., Qin *et al.*, 2019). To identify the sensitivity of surface property, a

628 histogram was constructed of difference between GEMS AEH and TROPOMI ALH

629   after classification into land and ocean surface types, as shown in Figure 16. From the

630   statistical results, the mean differences were estimated to be 1.12 ± 1.20 and 1.92 ± 1.06

631   km for ocean and land pixels, respectively. The bias has significant difference between

632   two different surface types. Michailidis et al. (2023) explained that the experimental

633   retrieval range of ALH from TROPOMI is 0.27-6.5 km and 0.06-2.15 km over ocean

634   and land, respectively. Constrained retrieval range over land by the TROPOMI

635   influences the negative bias of aerosol height retrieval and increases the mean difference

636   of aerosol height between GEMS and TROPOMI. In addition, the non-Lambertian

637   effect for surface reflectance is also affecting the increasing discrepancy of aerosol

638   height information.

639
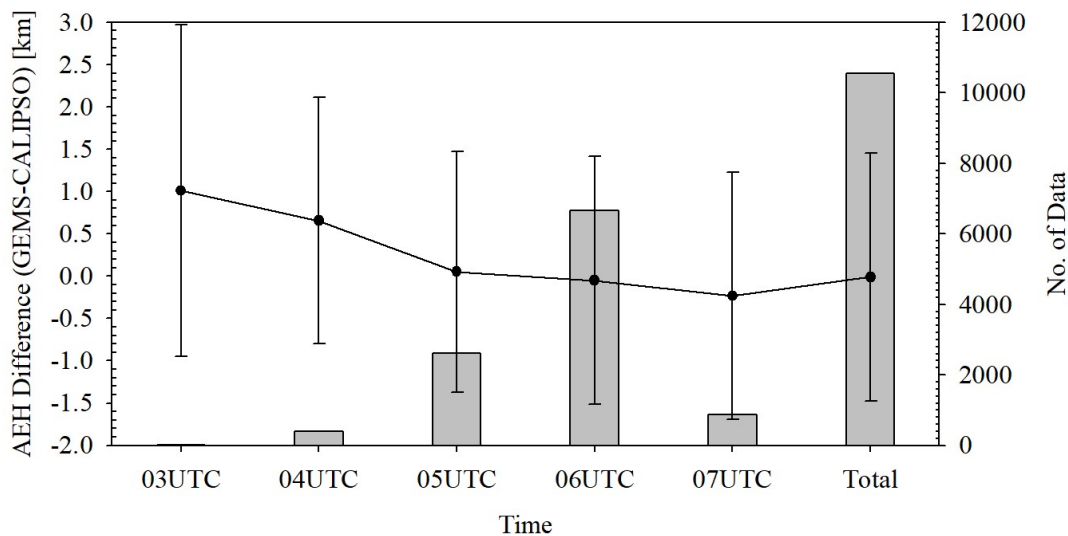
640   **Figure 17.** Diurnal dependence of AEH difference between CALIOP and GEMS

641   from January 1 to June 30, 2021 (Black dots and error bars denote the mean and

642   standard deviation of AEH difference, while the gray-box indicates the number of data).

643

644   The results of hourly statistical analyses are presented in Figure 17. Because they use

645   a consistent definition of AEH, we show only a comparison of GEMS and CALIOP. The

646   diurnal variation in AEH difference ranged from -0.23 ± 1.45 km (07:00 UTC, Number

647   of Data = 867) to 1.01 ± 1.96 km (03:00 UTC, Number of Data = 23). However, the

648   number of pixels observed at 03:00 UTC was insufficient for the identification of

649   diurnal variation of retrieval uncertainty. The AEH difference of 0.66 ± 1.45 km was the

650   next highest value obtained at 04:00 UTC (Number of Data = 395). The inhomogeneous

651   number of data is mainly due to the lack of spatial homogeneity among retrieval pixels.

652   Over India, very high AOD values were consistently observed during the comparison

653   period. Otherwise, the AEH was only retrieved under conditions of severe

654   anthropogenic emissions over East Asia. In addition, the diurnal variation in AEH

655   difference was caused by spatial characteristics of AEH difference. From 03:00 to 05:00

656   UTC, CALIOP mainly passed over East Asia, which has numerous sources of aerosol

657   emissions, including biomass burning, dust, and industrial activity. In addition, GEMS

658   observed only the eastern part of India, which is dominated by anthropogenic aerosols.

659   The spatial distribution of the dominant aerosol types may impact the diurnal variation

660   in AEH difference.

661

662   **6. Summary & Conclusions**

663   Based on the possibility of retrieving AEH from environmental satellite sensors, an

664   AEH retrieval algorithm for GEMS was developed that solely uses the O_2-O_2 absorption

665   band with considering of aerosol and surface properties. Because the sensitivity of AEH

666   retrieval is strongly affected by optical depth and properties of aerosols, as well as

667   surface reflectivity, the AEH retrieval algorithm for GEMS uses the GEMS operational

668   product, L2AERAOD. With the newly developed retrieval algorithm, GEMS can be

669   used to monitor aerosol vertical information with high temporal and spatial resolution.

670   For dust plumes over East Asia, AEH retrieval results from GEMS indicated

671   appropriated aerosol vertical information. After spatial and temporal colocation, the

672   AEH from GEMS aligned well with the AEH information obtained from CALIOP. The

673   differences in AEH between GEMS and CALIOP for dust plume cases were -0.13 ±

674   1.32 and -0.15 ± 0.97 km, with 49.9-75.9% and 73.2-86.7% of all pixels showing

675   differences less than 1.0 and 1.5 km, respectively. Large AEH uncertainty was found

676   mostly over inland China due to uncertainty in surface reflectance and AOD over the

677   land surface. In addition, AEH from GEMS was overestimated compared to the

678   TROPOMI ALH results. The overestimation is partially caused by different definitions

679   of ALH from TROPOMI and AEH from GEMS.

680   In long-term intercomparison with CALIOP, the average AEH difference was

681   estimated to be -0.03 km, with a standard deviation of 1.4 km under the scenario of

682   AOD > 0.4. The large variation in AEH difference between GEMS and CALIOP was

683   caused by uncertainty in the input parameters estimated from L2AERAOD. In the long-

684   term intercomparison against TROPOMI, this difference was dependent on both SSA

685   and TYPE. The difference was 1.50 ± 1.08 km, 1.59 ± 1.22 km, and 1.71 ± 1.24 km for

686   pixels with SSA < 0.90, 0.90 < SSA < 0.95, and SSA > 0.95, respectively. In addition,

687   differences of 1.47 ± 1.15 km, 1.46 ± 0.98 km, and 1.80 ± 1.32 km were obtained for

688   the "Absorbing", "Dust", and the "Non-Absorbing" types of aerosols, respectively. The

689   AEH difference also has diurnal dependence, which ranged from -0.23 ± 1.45 km to

690   1.01 ± 1.96 km, due to the spatial characteristics of dominant aerosol types.

691   The case studies and results of the long-term validation show that AEH retrieved

692   from GEMS can provide information on aerosol vertical distribution, with applications

693 in diverse research fields. The AEH results with long-term statistical accuracy make it

694 possible to use the application study for AMF calculation of GEMS trace gas retrieval.

695 In addition, AEH considerably affects the surface particulate matter (PM) concentration

696 obtained from satellite-based AOD because PM estimation is significantly affected by

697 the mixing layer height of aerosols. For this reason, the AEH can provide effective

698 mixing layer height of aerosols for anthropogenic aerosols and also provide the vertical

699 patterns for long-range transport of aerosols.

700 Although several fields of study may apply the AEH retrieval results, retrieval

701 uncertainty in AEH remains due to the uncertainty of retrieved AOD and SSA. In

702 addition, the uncertainty in surface reflectance and the discrepancy in O_2-O_2 SCD

703 values between the simulation results and observations can be affected to the potential

704 error sources of AEH from GEMS. To minimize the AEH retrieval uncertainty, further

705 analysis related to the optimized input parameters of AOD, SSA, and aerosol type

706 information is essential. For this reason, the quantitative analysis of AEH uncertainty

707 due to aerosol and surface property is important for the improvement of AEH retrieval

708 algorithm. In addition, aerosol optical property retrieval by the visible channel will be

709 needed for further study to improve the aerosol type determination. Although the

710 aerosol indices of UV and visible provide the aerosol type information, developing the

711 aerosol type classification algorithm is necessary to make synergy with AEH retrieval.

712 AEH provides representative layer height information as only one variable because of

713 its sole reliance on O_2-O_2 SCD for direct estimation of aerosol height information. This

714 method is limited to the consideration of aerosol vertical structures (i.e., Gaussian or

715 exponential vertical distribution structures). To increase the information contents, it

716 would be valuable to combine other oxygen absorption bands from other satellite

717   instruments together with extinction information of aerosols.

718

719   **Data Availability**

720   The TROPOMI ALH product is available from http://doi.org/10.5270/S5P-7g4iapn,

721   and the CALIOP aerosol extinction profile product is available from

722   https://doi.org/10.5067/CALIOP/CALIPSO/CAL_LID_L2_05kmAPro-Prov-V3-41.

723   The GEMS AEH and AERAOD products are available from the Environmental Satellite

724   Center in National Institute of Environmental Research (NIER) of the Republic of

725   Korea.

726

727   **Author Contributions**

728   SP, JK, and HL contributed to the design and implementation of this research. SP

729   developed the methodology and writing of the manuscript. YC and JP contributed the

730   software development and validation. DL, WL, and DK contributed the resources.

731

732   **Competing Interests**

733   The contact author has declared that none of the authors has any competing interests.

734

735   **Acknowledgements**

736   This work was supported by the National Institute of Environment Research of the

737   Republic of Korea under Grant NIER-2023-04-02-050.

738

739 **References**

740 Accarreta, J. R., de Haan, J. F., and Stammes, P.: Cloud pressure retrieval using the O2-
741   O2 absorption band at 477 nm, J. Geophys. Res., 109, D05204,
742   doi:10.1029/2003JD003915, 2004

743 Ahn, C., Torres, O., and Jethva, H.: Assessment of OMI near-UV aerosol optical depth
744   over land, J. Geophys. Res., 119, 2457-2473, 2014.

745 Bogumil, K., Orphal, J., Burrows, J. P., and Flaud, J. M.: Vibrational progressions in the
746   visible and near-ultraviolet absorption spectrum of ozone, Chem. Phys. Lett., 349,
747   241-248, 2001.

748 Buchard, V., de Silva, A. M., Colarco, P. R., Darmenov, A., Randles, C. A., Govindaraju,
749   R., Torres, O., Campbell, J., and Spurr, R.: Using the OMI aerosol index and
750   absorption aerosol optical depth to evaluate the NASA MERRA Aerosol reanalysis,
751   Atmos. Chem. Phys., 15, 5743-5760, 2015.

752 Chen, X., Wang, J., Xu, X., Zhou, M., Zhang, H., Garcia, L. C., Colarco, P. R., Janz, S.
753   J., Yorks, J., McGill, M., Reid, J. S., de Graaf, M., and Kondragunta, S.: First
754   retrieval of absorbing aerosol height over dark target using TROPOMI oxygen B
755   band: Algorithm development and application for surface particulate matter
756   estimates, Remote Sens. Env., 265, 112674, 2021.

757 Chen, X., Xu, X., Wang, J., and Diner, D. J.: Can Multi-angular polarimetric
758   measurements in the oxygen-A and B bands improve the retrieval of aerosol
759   vertical distribution?, J. Quant., Spectro. Rad. Trans., 270, 107679, 2021.

760 Chimot, J., Veefkind, J. P., Vlemmix, T., de Haan, J. F., Amiridis, V., Proestakis, E.,
761   Marinou, E., and Levelt, P. F.: An exploratory study on the aerosol height retrieval
762   from OMI measurements of the 477 nm O2-O2 spectral band using a neural
763   network approach, Atmos. Meas. Tech., 10, 783-809, 2017.

764 Choi, H., Liu, X., Abad, G. G., Seo, J., Lee, K. -M., and Kim, J.: A fast retrieval of
765   cloud parameters using a Triplet of wavelengths of oxygen dimer band around 477
766   nm, Remote Sens., 13, 152, doi: 10.3390/rs13010152, 2021.

767 Choi, W., Lee, H., Kim, J., Ryu, J. -Y., Park, S. S., Park, J., and Kang, H.: Effects of
768   spatiotemporal O4 column densities and temperature-dependent O4 absorption
769   cross-section on an aerosol effective height retrieval algorithm using the O4 air

770   mass factor from the ozone monitoring instrument, Remote Sens. Env., 229, 223-
771   233, 2019.

772   Choi, W., Lee, H., and Kim, J.: First TROPOMI retrieval of aerosol effective height
773   using O4 absorption band at 477 nm and aerosol classification, IEEE Trans.
774   Geosci., Remote Sens., 59, 9873-9886, 2021.

775   de Graaf, M., Stammes, P., Torres, O., and Koelemeijer, R. B. A.: Absorbing aerosol
776   index: Sensitivity analysis, application to GOME and comparison with TOMS, J.
777   Geophys. Res., 110, D01201, doi:10.1029/2004JD005178, 2005.

778   de Graaf, M., de Haan, J. F., and Sanders, A. F. J.: TROPOMI ATBD of the Aerosol
779   Layer   Height,   issue   2.4.0,   2022-04-08,
780   https://sentinel.esa.int/documents/247904/2476257/Sentinel-5P-TROPOMI-
781   ATBD-Aerosol-Height, 75pp, Royal Netherlands Meteorological Institute,
782   Netherland, last access: 15 June, 2024.

783   Ding, S., Wang, J., and Xu, X.: Polarimetric remote sensing in oxygen A and B bands:
784   Sensitivity study and information content analysis for vertical profile of aerosols,
785   Atmos. Meas. Tech, 9, 2077-2092, 2016.

786   Dubuisson, P., Frouin, R., Dessaily, D., Duforet, L., Leon, J. –F., Voss, K., and Antoine,
787   D.: Estimating the altitude of aerosol plumes over the ocean from reflectance ratio
788   measurements in the O2 A-band, Remote Sens. Environ., 113, 1899-1911,
789   doi:10.1016/j.rse.2009.04.018, 2009.

790   European Space Agency, *TROPOMI Level 2 Aerosol Layer Height products. Version*
791   *02.* https://doi.org/10.5270/S5P-7g4iapn, 2021.

792   Gao, Y., Zhao, C., Liu, X., Zhang, M., and Leung, L. R.: WRF-Chem simulations of
793   aerosols and anthropogenic aerosol radiative forcing in East Asia, Atmos. Environ.,
794   92, 250-266, 2014.

795   Geddes, A., and Boesch, H.: Tropospheric aerosol profile information from high-
796   resolution oxygen A-band measurements from space, Atmos. Meas. Tech., 8, 859-
797   874, 2015.

798   Go, S., Kim, J., Park, S. S., Kim, M., Lim, H., Kim, J. -Y., Lee, D. -W., and Im, J.:
799   Synergistic use of hyperspectral UV-visible OMI and broadband meteorological
800   imager MODIS data for a merged aerosol product, Remote Sens., 12, 3987,
801   doi:10.3390/rs12233987, 2020.

802 Griffin, D., Sioris, C., Chen, J., Dickson, N., Kovachik, A., de Graaf, M., Nanda, S.,
803   Veefkind, P., Dammers, E., McLinden, C. A., Makar, P., and Akingunola, A.: The
804   2018 fire season in North America as seen by TROPOMI: aerosol layer height
805   intercomparisons and evaluation of model-derived plume heights, Atmos. Meas.
806   Tech., 13, 1427-1445, 2020.

807 Herman, J. R., Bhartia, P. K., Torres, O., Hsu, C., Seftor, C., and Celarier, E.: Global
808   distribution of UV-absorbing aerosols from Nimbus-7/TOMS data, J. Geophys.
809   Res., 102(D14), 16911-16922, 1997.

810 Hong, H., Lee, H., Kim, J., Jeong, U., Ryu, J., and Lee, D. S.: Investigation of
811   simultaneous effects of aerosol properties and aerosol peak height on the air mass
812   factors for space-borne NO2 retrievals, Remote Sens., 9, 208,
813   doi:10.3390/rs9030208, 2017.

814 Joiner, J., and Bhartia, P. K.: The determination of cloud pressures from rotational
815   Raman scattering in satellite backscatter ultraviolet measurements, J. Geophys.
816   Res., 100, 23019-23026, 1995.

817 Joiner, J., and Vasilkov, A. P.: First results from the OMI rotational Raman scattering
818   cloud pressure algorithm, IEEE Trans. Geosci. Remote Sens., 44, 1272-1282, 2006.

819 Kim, M., Kim, J., Torres, O., Ahn, C., Kim, W., Jeong, U., Go, S., Liu, X., Moon, K. J.,
820   and Kim D. -R.: Optimal estimation-based algorithm to retrieve aerosol optical
821   properties for GEMS measurements over Asia, 10, 162, doi:10.3390/rs10020162,
822   2018.

823 Kim, J., Jeong, U., Ahn, M. -H., Kim, J. H., Park, R. J., Lee, H., Song, C. H., Choi, Y. -
824   S., Lee, K. -H., Yoo, J. -M., Jeong, M. -J., Park, S. K., Lee, K. -M., Song, C. -K.,
825   Kim, S. -W., Kim, Y. J., Kim, S. -W., Kim, M., Go, S., Liu, X., Chance, K., Chan
826   Miller, C., Al-Saadi, J., Veihelmann, B., Bhartia, P. K., Torres, O., González Abad,
827   G., Haffner, D. P., Ko, D. H., Lee, S. H., Woo, J. -H., Chong, H., Park, S. S., Nicks,
828   D., Choi, W. J., Moon, K. -J., Cho, A., Yoon, J., Kim, S. -K., Hong, H., Lee, K.,
829   Lee, H., Lee, S., Choi, M., Veefkind, P., Levelt, P. F., Edwards, D. P., Kang, M., Eo,
830   M., Bak, J., Baek, K., Kwon, H. -A., Yang, J., Park, J., Han, K. M., Kim, B. -R.,
831   Shin, H. -W., Choi, H., Lee, E., Chong, J., Cha, Y., Koo, J. -H., Irie, H., Hayashida,
832   S., Kasai, Y., Kanaya, Y., Liu, C., Lin, J., Crawford, J. H., Carmichael, G. R.,
833   Newchurch, M. J., Lefer, B. L., Herman, J. R., Swap, R. J., Lau, A. K. H., Kurosu,

T. P., Jaross, G., Ahlers, B., Dobber, M., McElroy, C. T., and Choi, Y.: New era of air quality from Space: Geostationary Environment Monitoring Spectrometer (GEMS), Bul. Ame. Meteorol. Soc., 101(1), E1–E22, 2020.

Koffi, B., Schulz, M., Bréon, F.-M., Griesfeller, J., Winker, D., Balkanski, Y., Bauer, S., Berntsen, T., Chin, M., Collins, W. D., Dentener, F., Diehl, T., Easter, R., Ghan, S., Ginoux, P., Gong, S., Horowitz, L. W., Iversen, T., Kirkevåg, A., Koch, D., Krol, M., Myhre, G., Stier, P., and Takemura, T.: Application of the CALIOP layer product to evaluate the vertical distribution of aerosols estimated by global models: AeroCom phase I results, J. Geophys. Res.-Atmos., 117, D10201, https://doi.org/10.1029/2011jd016858, 2012.

Kokhanovsky, A. A., and Rozanov, V. V.: The determination of dust cloud altitudes from a satellite using hyperspectral measurements in the gaseous absorption band, Int. J. Rem. Sens., 31, Nos. 9-10, 2729-2744, 2010.

Kooreman, M. L., Stammes, P., Trees, V., Sneep, M., Tilstra, L. G., de Graaf, M., Zweers, D. C. S., Wang, P., Tuinder, O. N. E., and Veefkind, J. P.: Effects of cloud on the UV absorbing aerosol index from TROPOMI, Atmos. Meas. Tech., 13, 6407-6426, 2020.

Lee, J., Kim, J., Song, C. H., Kim, S. B., Chun, Y., Sohn, B. J., and Holben, B. N.: Characteristics of aerosol types from AERONET sunphotometer measurements. Atmos. Env., 44, 3110-3117, 2010.

Lorente, A., Boersma, K. F., Yu, H., Doerner, S., Hilboll, A., Richter, A., Liu, M., Lamsal, L. N., Barkley, M., De Smedt, I., Van Roozendael, M., Wang, Y., Wagner, T., Beirle, S., Liu, J. -T., Krotkov, N., Stammes, P., Wang, P., Eskes, H. J., and Krol, M.: Structural uncertainty in air mass factor calculation for NO2 and HCHO satellite retrieval, Atmos. Meas. Tech., 10, 759-782, 2017.

Michailidis, K., Koukouli, M. -E., Balis, D., Veefkind, J. P., de Graaf, M., Mona, L., Papagianopoulos, N., Pappalardo, G., Tsikoudi, I., Amiridis, V., Marinou, E., Gialitaki, A., Mamouri, R. -E., Nisantzi, A., Bortoli, D., Joao Costa, M., Salgueiro, V., Papayannis, A., Mylonaki, M., Alados-Arboledas, L., Romano, S., Perrone, M. R., and Baars, H.: Validation of the TROPOMI/S5P aerosol layer height using EARLINET lidars, Atmos. Chem. Phys., 23, 1919-1940, 2023.

865   Nanda, S., de Graaf, M., Sneep, M., de Haan, J. F., Stammes, P., Sanders, A. F. J.,

866   Tuinder, O., Veefkind, J. P., and Levelt, P. F.: Error sources in the retrieval of

867   aerosol information over bright surfaces from satellite measurements in the oxygen

868   A band, Atmos. Meas. Tech., 11, 161–175, https://doi.org/10.5194/amt-11-161-

869   2018, 2018.

870   Nanda, S., de Graaf, M., Veefkind, J. P., Sneep, M., ter Linden, M., Sun, J., and Level, P.

871   F.: A first comparison of TROPOMI aerosol layer height (ALH) to CALIOP data,

872   Atmos. Meas. Tech., 13, 3043-3059, 2020.

873   National Institute of Environmental Research, Geostationary Environment Monitoring

874   Spectrometer (GEMS) Algorithm Theoretical Basis Document: Aerosol Retrieval

875   Algorithm, 42pp, Ministry of Environment, Korea, 2020.

876   Omar, A., Winker, D. M., Vaughan, M. A., Ju, Y., Trepte, C. R., Ferrare, R. A., Lee, K.-

877   P., Hostetler, C. A., Kittaka, C., Rogers, R. R., Kuehn, R. E., and Liu, Z.: The

878   CALIPSO automated aerosol classification and Lidar ratio selection algorithm, J.

879   Atmos. Ocean. Tech., 26, 10, 1994-2014, 2009.

880   Park, S. S., Kim, J., Lee, H., Torres, O., Lee, K. –M., and Lee, S. D.: Utilization of O4

881   slant column density to derive aerosol layer height from a space-borne UV-visible

882   hyperspectral sensor: Sensitivity and case study, Atmos. Chem. Phys., 16, 1987-

883   2006, doi:10.5194/acp-16-1987-2016, 2016.

884   Park, S. S., Takemura, T., and Kim, J.: Effect of temperature-dependent cross sections

885   on O4 slant column density estimation by a space-borne UV-visible hyperspectral

886   sensor, Atmos. Environ., 152, 98-110, 2017.

887   Park, S. S., Kim, S. -W., Song, C. -K., Park, J. -U., and Bae, K. -H.: Spatio-temporal

888   variability of aerosol optical depth, total ozone, and NO2 over East Asia: Strategy

889   for the validation to the GEMS Scientific Products, Remote Sens., 12, 2256, 2020.

890   Peng, J., Hu, M., Guo, S., Du, Z., Zheng, J., Shang, D., Zamora, M. L., Zeng, L., Shao,

891   M., Wu, Y. -S., Zheng, J., Wang, Y., Glen, C. R., Collins, D. R., Molina, M. J., and

892   Zhang R.: Markedly enhanced absorption and direct radiative forcing of black

893   carbon under polluted urban environments, Proc. Natl. Acad. Sci., 113, 4266-4271,

894   2016.

895   Penning de Vries, M. J. M., Beirle, S., and Wagner, T.: UV aerosol indices from
896   SCIAMACHY: Introducing the Scattering Index (SCI), Atmos. Chem. Phys., 9,
897   9555-9567, 2009.

898   Penning de Vries, M. J. M., Beirle, S., Hoermann, C., Kaiser, J. W., Stammes, P., Tilstra,
899   L. G., Tuinder, O. N. E., and Wagner, T.: A global aerosol classification algorithm
900   incorporating multiple satellite data sets of aerosol and trace gas abundances,
901   Atmos. Chem. Phys., 15, 10597-10618, 2015.

902   Prospero, J. M., Ginoux, P., Torres, O., Nicholson, S. E., and Gill T. E.: Environmental
903   characterization of global sources of atmospheric soil dust identified with the
904   Nimbus 7 total ozone mapping spectrometer (TOMS) absorbing aerosol product,
905   Rev. Geophys., 40, 1002, doi:10.1029/2000RG000095, 2002.

906   Qin, W., Fasnacht, Z., Haffner, D., Vasilkov, A., Joiner, J., Krotkov, N., Fisher, B., and
907   Spurr, R.: A geometry-dependent surface Lambertian-equivalent reflectivity
908   product for UV-vis retrievals – Part 1: Evaluation over land surfaces using
909   measurements from OMI at 466 nm, Atmos. Meas. Tech., 12, 3997-4017, 2019.

910   Rana, A., Jia, S., and Sarkar, S.: Black carbon aerosol in India: A comprehensive review
911   of current status and future prospects, Atmos. Res., 218, 207-230, 2019.

912   Sanders, A. F. J., de Haan, J. F., Sneep, M., Apituley, A., Stammes, P., Vieitez, M. O.,
913   Tilstra, L. G., Tuinder, O. N. E., Koning, C. E., and Veefkind, J. P.: Evaluation of
914   the operational Aerosol Layer Height retrieval algorithm for Sentinel-5 Precursor:
915   application to O2 A band observations from GOME-2A, Atmos. Meas. Tech., 8,
916   4947-4977, 2015.

917   Sanders, A. F. J. and de Haan, J. F.: TROPOMI ATBD of the Aerosol Layer Height
918   product, 2016.

919   Sanghavi, S., Martonchik, J. V., Landgraf, J., and Platt, U.: Retrieval of optical depth
920   and vertical distribution of particulate scatterers in the atmosphere using O2 A- and
921   B-band SCIAMACHY observations over Kanpur: A case study, Atmos. Meas.
922   Tech., 5, 1099-1119, 2012.

923   Spurr, R. "User's Guide VLIDORT Version 2.6, RT Solutions.", Cambridge, MA,
924   USA, 2013.

925   Spurr, R., and Christri, M.: On the generation of atmospheric property Jacobians from
926   the (V)LIDORT linearized radiative transfer models, J. Quant. Spectrosc. Radiat.
927   Transf., 142, 109-115, 2014.

928   Thalman, R., and Volkamer, R.: Temperature dependent absorption cross-sections of
929   O2-O2 collision pairs between 340 and 630 nm and at atmospherically relevant
930   pressure. Phys. Chem. Chem. Phys. 15, 15371e15381, 2013.

931   Torres, O., Bhartia, P. K., Herman, J. R., Ahmad, Z., and Gleason, J.: Derivation of
932   aerosol properties from satellite measurements of backscattered ultraviolet
933   radiation: Theoretical basis, J. Geophys. Res., 103(14), 17099-17110, 1998.

934   Torres, O., Decae, R., Veefkind, P., and de Leeuw, G.: OMI Aerosol Retrieval Algorithm,
935   OMI Algorithm Theoretical Basis Document, Vol. III, Clouds, Aerosols and
936   Surface UV Irradiance, NASA-KNMI ATBD-OMI-03, pp. 47-71, 2002.

937   Torres, O., Jethva, H., Ahn, C., Jaross, G., and Loyola, D. G.: TROPOMI aerosol
938   products: evaluation and observations of synoptic-scale carbonaceous aerosol
939   plumes during 2018-2020, Atmos. Meas. Tech., 13, 6789-6806, 2020.

940   Vandaele, A. C., Hermans, C., Simon, P. C., Carleer, M., Colin, R., Fally, S., Merienne,
941   M. F., Jenouvrier, A., and Coquart, B.: Measurements of the NO2 absorption cross-
942   section from 42000 cm-1 to 10000 cm-1 (238-1000 nm) at 220 K and 294 K, J.
943   Quant. Spectrosc. Radiat. Transfer, 59, 3-5, 171-184, 1998.

944   Vasilkov, A., Joiner, J., Spurr, R., Bhartia, P. K., Levelt, P., and Stephens, G.: Evaluation
945   of the OMI cloud pressures derived from rotational Raman scattering by
946   comparisons with other satellite data and radiative transfer simulations, J. Geophys.
947   Res., 113, D15S19, doi:10.1029/2007JD008689, 2008.

948   Vasilkov, A., Yang, E. -S., Marchenko, S., Qin, W., Lamsal, L., Joiner, J., Krotkov, N.,
949   Haffner, D., Bhartia, P. K., and Spurr, R.: A cloud algorithm based on the O2-O2
950   477 nm absorption band featuring an advanced spectral fitting method and the use
951   of surface geometry-dependent Lambertian-equivalent reflectivity, Atmos. Meas.
952   Tech., 11, 4093-4107, 2018.

953   Veefkind, J. P., Aben, I., McMullan, K., Foerster, H., de Vries, J., Otter, G., Claas, J.,
954   Eskes, H. J., de Haan, J. F., Kleipool, Q., van Weele, M., Hasekamp, O.,
955   Hoogeveen, R., Landgraf, J., Snel, R., Tol, P., Ingmann, P., Voors, R., Kruizinga, B.,
956   Vink, R., Visser, H., and Levelt, P. F.: TROPOMI on the ESA Sentinel-5 Precursor:

957   A GMES mission for global observations of the atmospheric composition for

958   climate, air quality and ozone layer applications, Remote Sens. Env., 120, 70-83,

959   2012.

960 Veihelmann, B., Levelt, P. F., Stammes, P., and Veefkind, J. P.: Simulation study of the

961   aerosol information content in OMI spectral reflectance measurements, Atmos.

962   Chem. Phys., 7, 3115-3127, 2007.

963 Wang, R., Tao, S., Wang, W., Liu, J., Shen, H., Shen, G., Wang, B., Liu, X., Li, W.,

964   Huang, Y., Zhang, Y., Lu, Y., Chen, H., Chen, Y., Wang, C., Zhu, D., Wang, X., Li,

965   B., Liu, W., and M, J.: Black carbon emissions in China from 1949 to 2050,

966   Environ., Sci. Technol., 46, 7595-7603, 2012.

967 Winker, D. M., Vaughan, M. A., Omar, A. H., Hu, Y., Powell, K. A., Liu, Z., Hunt, W.

968   H., and Young, S. A.: Overview of the CALIPSO mission and CALIOP data

969   processing algorithms, J. Atmos. Oceanic Technol., 26, 2310-2323, 2009.

970 Xu, X., Wang, J., Yang, Y., Zeng, J., Torres, O., Yang, Y., Marshak, A., Reid, J., and

971   Miller, S.: Passive remote sensing of altitude and optical depth of dust plumes

972   using the oxygen A and B bands: First results from EPIC/DSCOVR at Lagrange-1

973   point, Geophys. Res. Lett., 44, 7544-7554, 2017.

974 Xu, X., Wang, J., Wang, Y., Zeng, J., Torres, O., Reid, J. S., Miller, S. D., Martins, J. V.,

975   and Remer, L. A.: Detecting layer height of smoke aerosols over vegetated land

976   and water surfaces via oxygen absorption bands: hourly results from

977   EPIC/DSCOVR in deep space, Atmos. Meas. Tech., 12, 3269-3288, 2019.

978 Zeng, Z. -C., Chen, S., Natraj, V., Le, T., Xu, F., Merrelli, A., Crisp, D., Sander, S. P.,

979   and Yung, Y. L.: Constraining the vertical distribution of coastal dust aerosol using

980   OCO-2 O2 A-band measurements, Remote Sens. Env., 236, 111494, 2020.

981